Distributed Magnetic Attitude Control for Large Space Structures

Bonar Robb[a,*], Malcolm McRobb[a,1], Gilles Bailet[a], James Beeley[a], Colin McInnes[a]

[a] *James Watt School of Engineering, James Watt (South) Building, University of Glasgow, Glasgow, Scotland G12 8QQ*

Abstract

The utility of distributed magnetic torque rods for the attitude control of a large space structure is investigated. Distributed arrays of actuators offer advantages such as distributing structural loads, increasing fault tolerance, allowing structures to be designed modularly, and additionally the actuators may be integrated with on-orbit fabrication strategies. First, distributed torques are shown to effectively rotate highly flexible structures. This is compared with torques applied to the centre-of-mass of the structure, which cause large surface deformations and can fail to enact a rotation. This is demonstrated using a spring-mass model of a planar structure with embedded actuators. A distributed torque algorithm is then developed to control an individually addressable array of actuators. Attitude control simulations are performed, using the array to control a large space structure, again modelled as a spring-mass system. The attitude control system is demonstrated to effectively detumble a representative 75×75 m flexible structure, and perform slew manoeuvres, in the presence of both gravity-gradient torques and a realistic magnetic field model.

Nomenclature

Angular velocity	=	$\boldsymbol{\omega}$
Areal mass-density	=	σ
Bdot control gain	=	k_{Bdot}
Body frame	=	$x_1 y_1 z_1$
Control reference torque	=	$\boldsymbol{T}_{ref}$
Cross sectional area	=	A
Damping coefficient	=	γ
Derivative gain	=	P_ω
Dipole moment to mass ratio	=	κ_τ
Earth-centred inertial frame	=	xyz
Error quaternion	=	$\boldsymbol{q}_{err}$
Force	=	$\boldsymbol{F}$
Inertia tensor	=	$\mathcal{I}$
Magnetic dipole moment	=	$\boldsymbol{m_d}$
Magnetic field	=	$\boldsymbol{B}$
Magnetorquer mass fraction	=	λ_f
Magnetorquer torque	=	$\boldsymbol{\tau}$
Natural length of spring	=	l_0
Number of activated magnetorquers	=	N_1, N_2
Particle mass	=	m_p
Position vector	=	$\boldsymbol{r}$

*Corresponding author

[1] Currently with Mangata Networks.

Position vector from primary body	=	$\boldsymbol{R}$
Proportional gain	=	P_q
Radius of Earth	=	R_E
Radius of enclosing circle	=	R_c
Reference magnetic field strength	=	B_0
Rotation matrix	=	$\mathcal{R}$
Second moment of area	=	I
Set of final particle positions	=	$\boldsymbol{q}$
Set of initial particle positions	=	$\boldsymbol{p}$
Spring constant	=	k
Standard gravitational parameter	=	μ
Structure side-length	=	d
Total actuation torque	=	$\boldsymbol{T}$
Total magnetorquer mass	=	M_τ
Total mass	=	M
Translation vector	=	$\boldsymbol{d}_t$
Young's modulus	=	E
ZYX intrinsic Euler angles	=	ψ, θ, ϕ

1. Introduction

Large space structures have been a subject of great interest within the spaceflight community, with potential applications including space-based solar power (SSP), orbital reflectors, large aperture telescopes and antennaes [1, 2], and solar sails [3] amongst others. Although a wide range of possible applications have been proposed, it is only in recent years that advances in additive manufacturing have incurred renewed interest in the possibility of fabricating large structures in-orbit [4, 5, 6, 7]. For example, recent work has considered magnetic attitude control for gossamer spacecraft through the use of a 3D printed, electrically conducting support structure [8]. This paper proposes a related concept, the use of distributed arrays of magnetic actuators for the attitude control of ultra-lightweight membrane reflectors or gossamer spacecraft.

Gossamer spacecraft have been actively developed by NASA, DLR and JAXA, primarily within the context of solar sailing. Consequently, research on gossamer spacecraft control has largely neglected magnetic attitude control, since an external magnetic field is required, making it unsuitable for the interplanetary trajectories of many solar sail missions. However, many applications of gossamer spacecraft exist in Earth-orbit, for which magnetic control may be a suitable candidate. One such application is SSP, a topic which has attracted considerable interest from the research community since the late 1960s and may play an important role in meeting future global energy needs [9]. Mankins et al. [10, 9, 11] provide an overview of the historical background of SSP, and in particular discuss the broad range of engineering challenges which have been considered. Many concepts for SSP-satellites have been proposed [12], and a common feature is large, high area-to-mass ratio solar collectors, allowing solar energy to be intercepted, converted to electricity and delivered to Earth via microwave transmission. Clearly, such solar collectors will require attitude control systems in order to remain Sun-pointing.

A closely related, or alternative, application to SSP is orbiting solar reflectors. Such orbital mirrors may be used to reflect sunlight to the Earth to illuminate densely populated areas or terrestrial solar PV-farms. This concept was studied by NASA in the 1970s, with further analysis concluding that the idea was not economically feasible at the time [13, 14]. More recent work examined the use of aluminised-Kapton films as solar mirrors and performed analysis of the film's mechanical and optical properties, with promising results [15, 16]. Lior [15] also performed an economic analysis, which agreed with the earlier NASA studies that the concept would not be economically viable unless transportation costs could be reduced to several hundred \$/kg. It is possible that falling launch costs and the development of in-orbit fabrication technologies may lead to growing interest in the orbital mirror concept in the future. Another use of orbiting solar reflectors is climate engineering [17, 18]. McInnes [19] provides an in-depth discussion of a number of ways in which

orbiting reflectors could be used to engineer the Earth's climate. These include the use of occulting disks at the Earth-Sun L_1 Lagrange point to partly block incoming solar radiation to offset the impact of human-driven climate change. While such macro-engineering projects may not be realised in the near-future, this remains an interesting area of research and adds to the range of applications for which gossamer spacecraft may be used.

A key requirement for orbital reflectors will be attitude control systems capable of orientating the spacecraft so that sunlight is continually reflected to a desired point on the Earth, or to direct sunlight to multiple points sequentially [20]. The geometry of the space mirror's orbit places stringent requirements on an attitude control system and the required angular accelerations it must deliver. NASA explored the use of reaction wheels for controlling an orbital mirror, a design that was considered feasible at the time [21]. Another NASA study, *SOLARES*, considered the use of flywheels affixed to a large reflector's supporting structure. One concept was to attach large flywheels which could be accelerated using solar radiation pressure (SRP) [22]. Once the wheels are sufficiently accelerated, control torques could be actuated by braking. The direct use of SRP is also often proposed as a means of attitude control, most commonly for solar sail applications. SRP can be used to induce control torques in a number of ways; proposed methods include controllable vanes [23, 24], gimbal systems to shift the centre-of-pressure on the sail [25], and more recently the use of surface reflectivity modulation [26, 27, 28]. The work of Borggräfe et al. [27] is particularly relevant to the strategy presented in this paper, as the authors show that a discrete grid of electro-chromic cells can be used for distributed attitude control of a gossamer spacecraft. In the model of Borggräfe et al. [27], a voltage can be applied to each cell which modifies its reflectivity. Attitude control is then achieved by finding combinations of activated cells that provide the desired torques on the spacecraft. This is similar to the model developed in this paper, where a grid of magnetorquers is used instead of reflective cells. However, a key difference between the actuators investigated in this paper and those investigated by Borggräfe et al. [27] is that magnetorquers only generate a torque on the spacecraft, rather than a force. A further difference is that in this paper it is assumed that the polarity of each magnetorquer can be reversed, resulting in three possible states, rather than the "on/off" cell states of Ref. [27]. Because of this, the look-up table method of Ref. [27], which is used to find control torques, is unsuitable for the magnetorquer model, leading to the torque distribution algorithm developed in Sec. III of this paper.

Distributed actuation in general has not been widely studied for large space structures. Hughes [29], Chee and Damaren [30], Hu et al. [31], and Damaren and D'Eleuterio [32] consider spacecraft with distributed gyricity, such as an array of control moment gyros, but these works are primarily concerned with shape control and vibration suppression. A notable exception is the recent work of Hu et al. [33], which integrates attitude control with vibration suppression for an array of reaction wheels. In our work we focus on distributed actuation specifically for the attitude control of large flexible structures, and aim to demonstrate that distributed torquing provides significant benefits over centralised torquing strategies. We then go on to consider the use of an array of magnetorquers for this purpose, a concept which we believe has not previously been considered in the literature. Magnetic torquers are a proven technology for spacecraft attitude control, but are often not considered for large space structures due to the large disturbance torques this class of spacecraft may experience. Polites et al. [34] discuss this issue, and show that with judicious orbit selection, control of a solar sail in low Earth orbit may be possible with reaction wheels and magnetorquers. An issue with the sole use of magnetic control for any spacecraft is that it cannot provide full 3-axis attitude control, as torques cannot be generated in the direction of the external magnetic field. However, this issue can be overcome in practice by performing sequences of manoeuvres or by considering that the external field direction changes over the course of an orbit, providing "average" controllability [35]. This is demonstrated by Lovera and Astolfi [36], and Yang [37], who investigate the stability conditions of magnetic actuation. Colagrossi and Lavagna [38] demonstrate the design of a fully magnetic attitude control system for picosat platforms, while further examples of magnetic attitude control system design are found in the survey of Ovchinnikov and Roldugin [35]. The use of magnetic attitude control for a large, gossamer spacecraft is considered by Robbins [39], who proposes the use of a large current loop for the attitude control of a 1500 m radio telescope.

The concept envisioned in this paper consists of a supporting substructure which may be 3d printed in-orbit and overlaid with a thin film membrane. As the structure is 3d printed, magnetorquers could be

integrated into the structure at regular intervals during fabrication, providing a distributed attitude control system, with the advantage of distributed torques and system redundancy. Such a structure may act as a solar sail for use in Earth orbit, or as a solar reflector, illuminating solar PV farms on Earth at times of peak demand, or illuminating populated areas [40, 41]. The spacecraft is modelled as a truss-like planar structure, with its mass concentrated at nodes connected by springs and dampers. In Sec. II, this model is presented and used to demonstrate the advantages of distributed torques by comparing the dynamics of flexible structures when acted upon by a large central torque or by an array of distributed torques. The aim of these simulations is to demonstrate that in general distributed attitude control torques have the advantage of reducing structural deformations. These results are then used to strengthen the case for the use of a distributed array of magnetorquers for attitude control. In Sec. III, a magnetorquer array is proposed in which two orthogonal magnetorquers are placed at each node of a square array. The problem of selecting and distributing the actuators in order to achieve a desired torque is addressed, and solved with the use of Voronoi diagrams and Lloyd's relaxation algorithm. Section IV then demonstrates the utility of such an array embedded within the spring-mass model, and is used to simulate detumbling and slew manoeuvres of a large, flexible structure in low Earth orbit (LEO). The aim of these orbital simulations is to demonstrate that a distributed magnetorquer array is capable of enacting 90 degree slew manoeuvres without inducing excessive structural deformation, despite the disturbing gravity gradient torque and time-varying magnetic field. Multiple simulations are performed here to demonstrate which manoeuvres can be achieved when operating within the geometric constraints of magnetic attitude control, given the changing directions of the magnetic field and gravity gradient torque relative to the spacecraft body-frame.

2. Distributed Control Torques for Large Space Structures

The motivation for distributed magnetorquer arrays is that it is assumed desirable to distribute actuator torques across the body of a large flexible space structure, in order to improve the attitude control system's effectiveness and reduce structural deformation. For a rigid body, a torque applied at a distance from the centre-of-mass is equivalent to one applied at the centre-of-mass. For a flexible body however, the location of torquing actuators and the induced flexible response is an important consideration when designing the attitude control system. In this section a spring-mass model representing a large, truss-like planar space structure is presented, and used to compare the flexible dynamics of distributed magnetorquer arrays with that of centralised torquing. Spring-mass or multi-particle models allow continuous structures to be modelled accurately with relatively low computational effort. They have been used extensively by JAXA for modelling the membrane dynamics of the IKAROS solar sail [42], and found to accurately predict the membrane dynamics when compared with flight-data. Here, a spring-mass model of a truss-structure is used as a generic model of a flexible, large space structure. The aim of this section is to demonstrate that for structures of the length-scale and flexibilities considered, distributed attitude control torques will reduce structural deformation when compared to centralised torquing. Later simulations are then used to demonstrate that an array of magnetorquers could serve this purpose, given the constraints and scaling laws unique to these actuators specifically.

2.1. Spring-Mass Model

The structure is modelled as a cubic lattice of nodes, connected by struts to give an octahedral-tetrahedral truss configuration, illustrated in Fig 1. This configuration is a common type of truss-structure used architecturally for wide-spanning roofs, due to its rigidity and high strength-to-weight ratio. [43] The mass of the structure is taken to be concentrated at these nodes, and the struts are approximated as linear, damped springs. The mechanical model is illustrated in Fig. 2. The spring force between connected particles is given by:

$$\boldsymbol{F}_s = k(r - l_0)\frac{\boldsymbol{r}}{r} + \gamma\left(\dot{\boldsymbol{r}} \cdot \frac{\boldsymbol{r}}{r}\right)\frac{\boldsymbol{r}}{r} \tag{1}$$

where k, γ and l_0 are the spring constant, damping coefficient, and natural length of the strut between the particles, and $\boldsymbol{r}$ and $\dot{\boldsymbol{r}}$ the relative position and velocity of neighbouring particles. The particle position

vectors and force directions are illustrated in Fig. 2. The total force on particle i due to the spring and dashpot is then found by summation over all connected particles:

$$\boldsymbol{F}_i^{\text{spring}} = \sum_{j \in C} \left[k(r_{ij} - l_0) \frac{\boldsymbol{r}_{ij}}{r_{ij}} + \gamma \left(\dot{\boldsymbol{r}}_{ij} \cdot \frac{\boldsymbol{r}_{ij}}{r_{ij}} \right) \frac{\boldsymbol{r}_{ij}}{r_{ij}} \right] \tag{2}$$

where the relative position of the particles is denoted by $\boldsymbol{r}_{ij} = \boldsymbol{r}_j - \boldsymbol{r}_i$, and C is the set of connected particles.

Actuator torques are included in the model by the appropriate application of forces to the individual particles. This work is concerned with magnetorquers, which produce a torque given by:

$$\boldsymbol{\tau} = \boldsymbol{m_d} \times \boldsymbol{B} \tag{3}$$

where $\boldsymbol{m_d}$ is the magnetic dipole moment of the magnetorquer, specified by the magnetorquer geometry and electrical current, and $\boldsymbol{B}$ is the external magnetic field. In the spring mass model, the mass is concentrated at the structure nodes as point masses, and so a torque cannot be applied to the nodes directly. To include these actuators, magnetorquers are placed between connected nodes, i.e. the magnetorquers are taken to be embedded within the connecting struts. If there is a magnetorquer rod embedded within the strut connecting particles i and j, its dipole moment is aligned with the strut and given by $\boldsymbol{m}_d = m_d \hat{\boldsymbol{r}}_{ij}$. The torque within the connecting element is experienced by the particles as a transverse force, given by:

$$\boldsymbol{F}_i^{\text{mag}} = -\boldsymbol{F}_j^{\text{mag}} = \frac{1}{r_{ji}} \left(m_d \boldsymbol{B} - \left(\frac{1}{2} m_d \boldsymbol{B} \cdot \hat{\boldsymbol{r}}_{ji} \right) \hat{\boldsymbol{r}}_{ji} \right) \tag{4}$$

This expression gives forces which are perpendicular to the connecting strut, and result in a torque around the centre of the strut which satisfies Eq. 3, i.e. $\frac{1}{2}\boldsymbol{r}_{ji} \times \boldsymbol{F}_i^{\text{mag}} + \frac{1}{2}\boldsymbol{r}_{ij} \times \boldsymbol{F}_j^{\text{mag}} = \boldsymbol{m}_d \times \boldsymbol{B}$.

The final force included in the model is gravity. The gravitational force on particle i is:

$$\boldsymbol{F}_i^{\text{grav}} = -\frac{\mu m_p}{R_i^2} \hat{\boldsymbol{R}}_i \tag{5}$$

where μ is the standard gravitational parameter of the primary body, m_p the particle mass, and $\boldsymbol{R}_i$ the absolute position vector expressed in a frame with origin at the centre of the primary body. The total force on particle i is given by summation of Eqs. 2, 4 and 5:

$$\boldsymbol{F}_i = \boldsymbol{F}_i^{\text{spring}} + \boldsymbol{F}_i^{\text{mag}} + \boldsymbol{F}_i^{\text{grav}} \tag{6}$$

Equation 6 is evaluated for all particles in the model, and the dynamics simulated by numerically integrating the position and velocity of all particles simultaneously. In the simulations, Runge-Kutta 4th order integration is used.

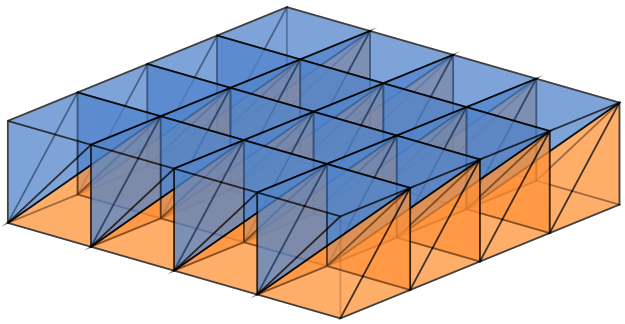

Figure 1: The octahedral-tetrahedral truss structure, the half octahedrons are highlighted in blue and orange with tetrahedrons filling the space in between.

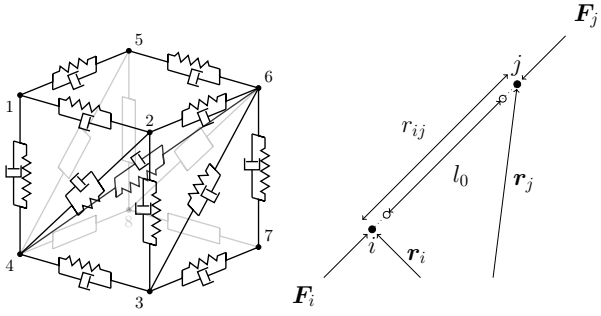

Figure 2: A cubic unit of the truss structure, showing the spring and dashpot connections between point masses at the numbered nodes, and the spring force directions for two displaced particles i and j.

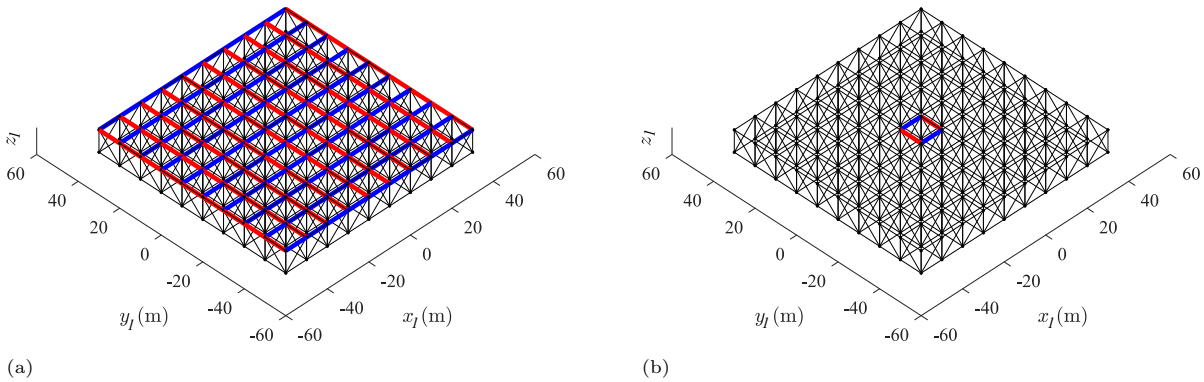

Figure 3: Example of the spring-mass model of the truss-structure with distributed (a) and centralised (b) torquing actuators. The x_1 and y_1 body axis actuators are highlighted in red and blue respectively.

2.2. Comparison of Distributed and Centralised Torques

The spring-mass model is now used to compare distributed and centralised torques by constructing a model of a planar structure with an embedded distributed array of torquing actuators, and one in which all torques are applied at the centre of the structure only. The two cases are illustrated in Fig. 3, which shows 40×40 m structures with actuators embedded in the blue and red highlighted elements. Figure 3a, shows actuators embedded within the struts between all nodes on the top layer of the structure, giving torques aligned with the x_1 and y_1 body axes. Figure 3b shows the same structure with actuators placed at the central cube unit only. Two highlighted elements are shown for each direction in the central case to maintain symmetry around the centre-of-mass. A 40×40 m structure is shown here to clearly illustrate the actuator location and directions, but in the following simulations a 100×100 m structure is also considered.

In this section, general torquing actuators are considered, rather than magnetorquers specifically, because the torque produced by a magnetorquer depends on its orientation relative to the magnetic field, according to Eq. 3. Furthermore, the magnetic field direction will be constantly changing while on-orbit. In this section, the aim is to investigate torque distribution across a flexible structure, and so assuming a constant torque for now allows direct comparison to be made between the distributed and centralised cases.

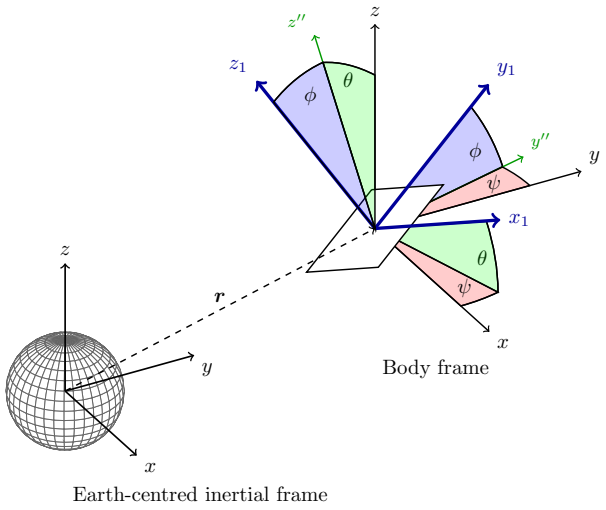

Figure 4: Earth-centred inertial frame, xyz, and sequence of rotations to the $x_1y_1z_1$ body frame.

A number of simulations are performed to compare distributed and centralised torques. Three structures are considered, with the spring constants adjusted to represent a range of structural flexibility. For each structure a simulation is performed with a single large torque applied to the centre of the structure, as illustrated in Fig. 3b, and then that same total torque is distributed across the grid of elements, as shown in Fig. 3a. The specific geometry used in the simulations is that of a 100 m side-length square structure, made up of a 19×19 grid of the unit cubes illustrated in Fig. 2, resulting in a side length for each cube of 5.26 m. The grid dimension of 19 is an odd number to ensure that a single cube lies at the centre of the structure, and so the centre-of-mass of the stucture lies in the centre of a unit cube rather than at a node. This means that, for centralised torquing, a torque can be applied to a single unit cube with the resulting torque symmetrical around the centre-of-mass of the structure, as illustrated in 3b. The torque applied is around the body frame x_1-axis. The $x_1y_1z_1$ body frame is initially aligned with the inertial xyz frame, shown in Fig. 3. Although the structure is actually a collection of particles, a body frame is defined by least-squares fitting a rotation between the initial particle positions and the displaced positions. The least-squares problem to minimise is

$$\min_{\mathcal{R},\boldsymbol{d}_t} \sum_{i=1}^{n} ||\mathcal{R}\boldsymbol{p}_i + \boldsymbol{d}_t - \boldsymbol{q}_i|| \tag{7}$$

where $\boldsymbol{p}_i$ and $\boldsymbol{q}_i$ are the initial and final set of points in the structure respectively, and $\mathcal{R}$ and $\boldsymbol{d}_t$ the rotation matrix and translation vector describing the mapping from $\boldsymbol{q}_i$ to $\boldsymbol{p}_i$. This problem can be solved using singular value decomposition, as described in Ref. [44]. The angular velocity body-rates of this rotating frame are then estimated using a backward difference formula, applied to the current best-fitting rotation matrix and that of the previous simulation timestep. Throughout the simulation, the standard ZYX intrinsic Euler angles ψ, θ, ϕ are used to represent the orientation of this body-frame. The sequence of rotations between the Earth-centred inertial frame and the body frame is illustrated in Fig. 4.

The structural mass, stiffness and magnitude of the actuator torques are selected by considering large solar sails, which may have areal densities of on the order of 10 g/m^2 [45]. This value is adopted for all three simulations, such that only the structural flexibility varies between the cases. For a 100×100 m structure, this results in a total mass of 100 kg. Commercial magnetorquers are available with a dipole moment to mass ratio of 100 Am^2/kg[46], and it is assumed that the maximum dipole moment of a magnetorquer scales linearly with its mass. If one third of the structural mass is allocated for magnetorquers, the maximum dipole moment is then taken to be 3333 Am^2. If the external magnetic field has a magnitude of 30 μT, such as may be found in low Earth orbit (LEO), the maximum achievable torque is found by applying Eq. 3, resulting in a representative torque of 0.1 Nm.

The model spring constant is determined by selecting a value for the overall bending stiffness of the structure. The bending stiffness of a four longeron truss with diagonal battens on each face is given by:

$$EI = 2EAR_c^2 \tag{8}$$

where E is the Young's modulus, A is the longeron cross sectional area and R_c is the radius of a circle enclosing the truss cross-section [47]. The structure considered here is comprised of 10 such trusses arranged in parallel, and so the total bending stiffness of the structure is found by multiplying Eq. 8 by 10, where any contribution of the connecting elements between layers is assumed to be negligible. The spring constants are related to EA by the formula $k = EA/l_0$, where l_0 is the natural length of the spring. Equation 8 treats the truss as an Euler beam, and so while the bending stiffness may be equivalent, other behaviour may not be well modelled by this approach. However, it is assumed to be a suitable approximation for the generic flexible structure modelled here. This process was verified by performing a cantilever test on the numerical model, where one side of the structure was held fixed and a load applied to the free end. The resulting deflection matched the expected value for a beam or plate with the specified bending stiffness. The most common solar sail design comprises diagonal booms supporting a tensioned membrane. The bending stiffness of these booms varies depending on the sail length-scale, but is generally on the order of 10^3 Nm^2. This bending stiffness is taken as the most rigid case to be examined. Cases two orders of magnitude lower are also investigated, to determine whether distributed torquing allows effective attitude control for even more flexible structures. As noted previously, the structural mass and the applied torque are held fixed

across the three cases considered to allow direct comparison of the results, but in practice a reduced bending stiffness would also be associated with a reduced structural mass.

Table 1 summarises the data which is common to all simulations. Simulations are performed over 30 minutes, denoted t_{end}, which is sufficient time for the structure to perform a significant rotation of at least 0.4 radians. A timestep, δt, of 0.1 s is selected for the Runge-Kutta integration, a value which was found to provide stable solutions with reasonable computation times. The torque profile described in Table 1 corresponds to a bang-bang-off signal, with the torque magnitude set to the maximum, $\tau_{\max}$, and the direction either positive or negative along the x_1 axis. Table 1 shows the three structural cases which are considered. The difference across each case is the spring constant used in the model, which is chosen such that the beam-like bending stiffness of the square structure, for bending around the x_1 or y_1 directions, is equal to 10^3, 10^2 and 10 Nm^2 for cases A, B and C respectively. These values correspond to the order of magnitude of bending stiffness of current solar sail designs (Case A), and two orders of magnitude lower. For the distributed torque case, the total mass of 100 kg is distributed between all particles, while for the central torque case one third of this mass, the fraction allocated for the actuators, is concentrated at the centre of the structure only.

If the structures were rigid bodies, the torque profile in Table 1 would result in a rest-to-rest manoeuvre. For the flexible structures considered here this control signal allows the response of the structure to be investigated when the torque is first applied and when it switches direction. Finally, when the torque is switched off the resulting residual vibrations in the structure can be observed as a measure of how much energy has been absorbed by the flexibility of the structure. For example, if the structure is found to have large amplitude residual vibrations it suggests that a significant portion of the control effort has been absorbed by the flexing structure as strain energy rather than working to rotate the structure. The surface standard deviation (SD), σ, is used as a measure of flatness in the following results, and is found by taking the average plane formed by the top layer of points in the structure, and then calculating the standard deviation of the normal distance of each particle to this plane. This measure of the surface flatness is of interest because if this parameter remains low then the structure is relatively un-deformed and is not likely to fail due to buckling. It is also important to consider this measure of surface flatness since many applications for space structures of this scale, such as reflectors, antennas, or solar power arrays would require a high degree of flatness during operation.

Side length	100 m
Structural units	20
Maximum torque, $\tau_{\max}$	0.1 Nm
Simulation runtime, t_{end}	30 minutes
Simulation timestep, δt	0.1s
Areal Density, σ	10 g/m^2
Total mass	100 kg
Particle mass, m_p	0.1250 kg (distributed)
	0.0833 kg (centralised)
Bending stiffness, EI	
Case A:	10^3 Nm^2
Case B:	10^2 Nm^2
Case C:	10^1 Nm^2
Torque Applied	$\tau_{\max}$ if $t \leq \frac{1}{3}t_{\text{end}}$
	$-\tau_{\max}$ if $\frac{1}{3}t_{\text{end}} < t \leq \frac{2}{3}t_{\text{end}}$
	0 if $t > \frac{2}{3}t_{\text{end}}$

Table 1: Parameters used for structural simulations.

2.3. Results of Simulation

Results of the simulations for Cases A, B and C with central and distributed torquing are shown in Figs. 6, 7 and 8 respectively. In all cases, distributed torquing results in a rigid-body like rotation of the structure. With central torquing however, a rigid-body like response is seen for Case A, but for more flexible structures much smaller rotations occur and the behaviour is less uniform, with rotations seen around axes other than the x_1 body axis. For Cases A and B, distributed torquing leads to an order of magnitude reduction in the surface SD, showing that distributed actuation has had the desired effect of reducing the surface deformation considerably.

For Case C the magnitude of the surface SD throughout simulation is comparable for both distributed and central torquing. Figure 5 shows the shape of the structure plotted at 500 s intervals. This shows that although the surface is deformed a comparable amount, with distributed torquing the deformation is much more uniform, creating a wave-like shape along the x_1 body axis. With central torquing the structure has points of high local deformation, particularly at the centre-of-mass where the torque is applied, and would therefore be more likely to fail due to buckling. Additionally, centralised torquing is unable to enact the desired rotation for Case C. This is because as the structure deforms, the orientation of the central points and thus the direction of the torque being applied is significantly altered, resulting in angular displacements around both the x_1 and y_1 body axes.

For distributed torquing, in the final third of the simulation the surface SD oscillates steadily with a small amplitude, which suggests that little energy has been absorbed as strain energy during torquing. With

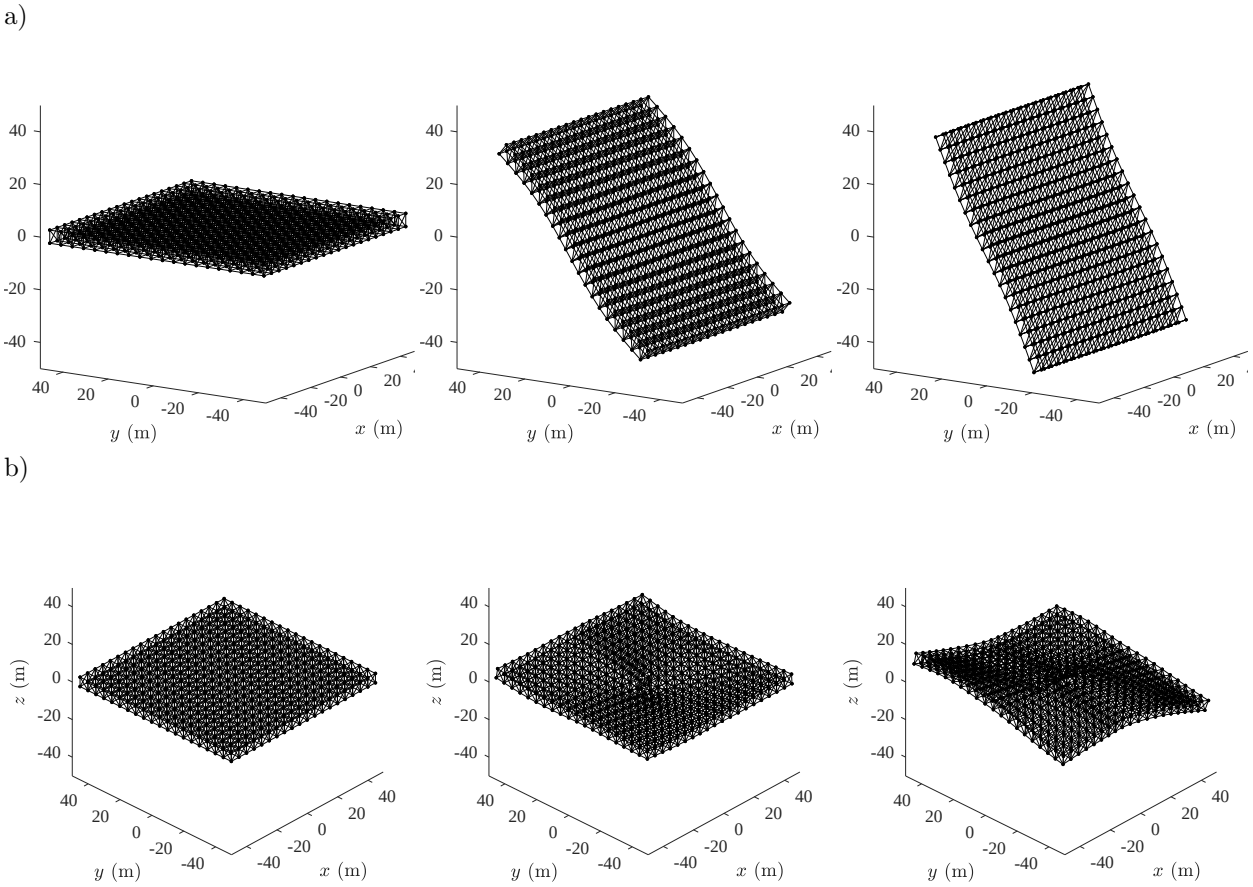

Figure 5: Structure shown in the inertial frame at 500 s intervals for Case C, after application of distributed (a) and central (b) torques.

central torquing, the surface SD is found to continue rising at this point. This is because the structure settles into a more uniform shape after the torque is switched off, which is a lower energy configuration despite having higher surface SD. Therefore the surface SD is not a direct measure of the potential energy in the spring-mass system because areas of high local deformation, such as the where the central torque is applied, can greatly contribute to the potential energy but not result in a large surface SD.

The "surface flatness" can also be measured by considering the angle the surface makes to the average plane at each point, which would be important if the surface were to be used as a reflector or solar sail as this would alter the local angle of incidence for incoming solar radiation. The local surface angle across the structure is determined by first fitting a continuous surface to the particle positions using a cubic interpolation, taking the gradient of this surface, and finally taking the inverse tangent to determine the angle between a plane tangent to the surface and the x_1y_1 plane, at each point of the interpolated surface. For the most rigid structure, Case A, there was little difference between rotations performed by central and distributed torquing, but there was a large difference in the surface SD for both cases. Further insight into this difference is gained by considering the local surface angle at the point of maximum surface SD, shown in Fig. 9. The figure shows that the order of magnitude reduction in surface SD achieved by distributed torquing corresponds to an order of magnitude reduction in the typical local surface angle as well. The figure also demonstrates that, for distributed torquing, the deformation is uniform along the x_1 axis, and the structure has settled into a wave-like shape, similar to Fig. 5a) but with a much smaller amplitude. For central torquing (a), the deformation is much less uniform, and the structure's edges make an angle of over 5° to the average plane. Of note is that the triangular artefacts visible in Fig. 9 are simply the effect of fitting a surface to the square units of the structure, and the large values at the structure's edges are a result of overfitting between the node positions.

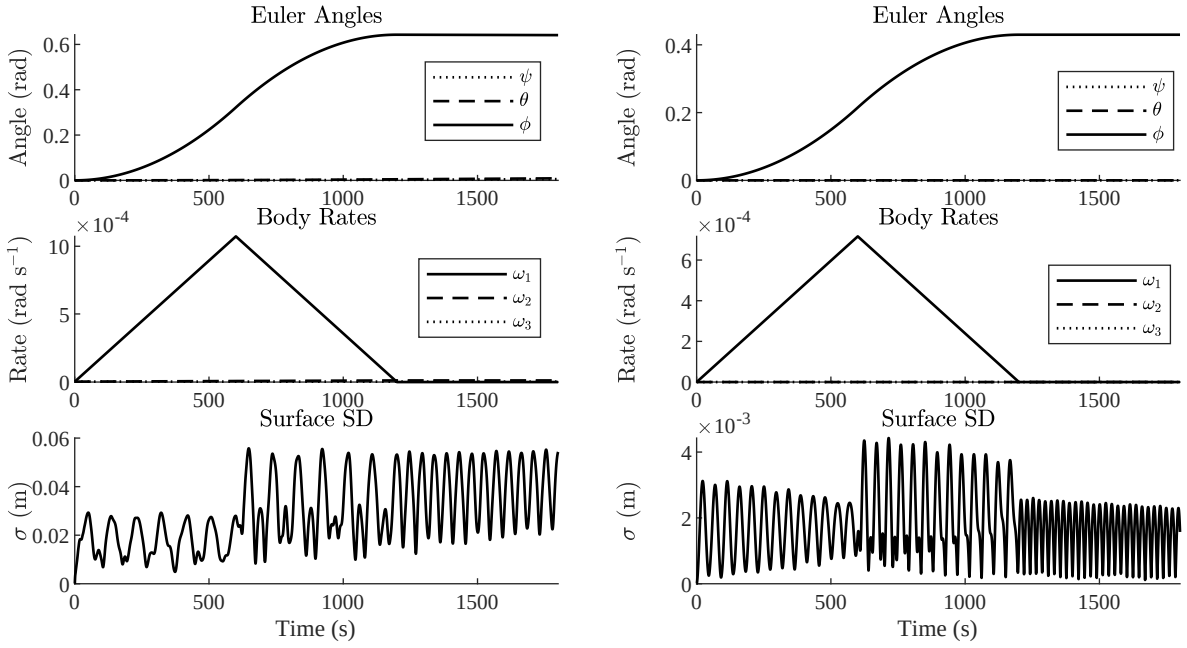

(a) Centralised torques.

(b) Distributed torques.

Figure 6: Results of simulation for Case A

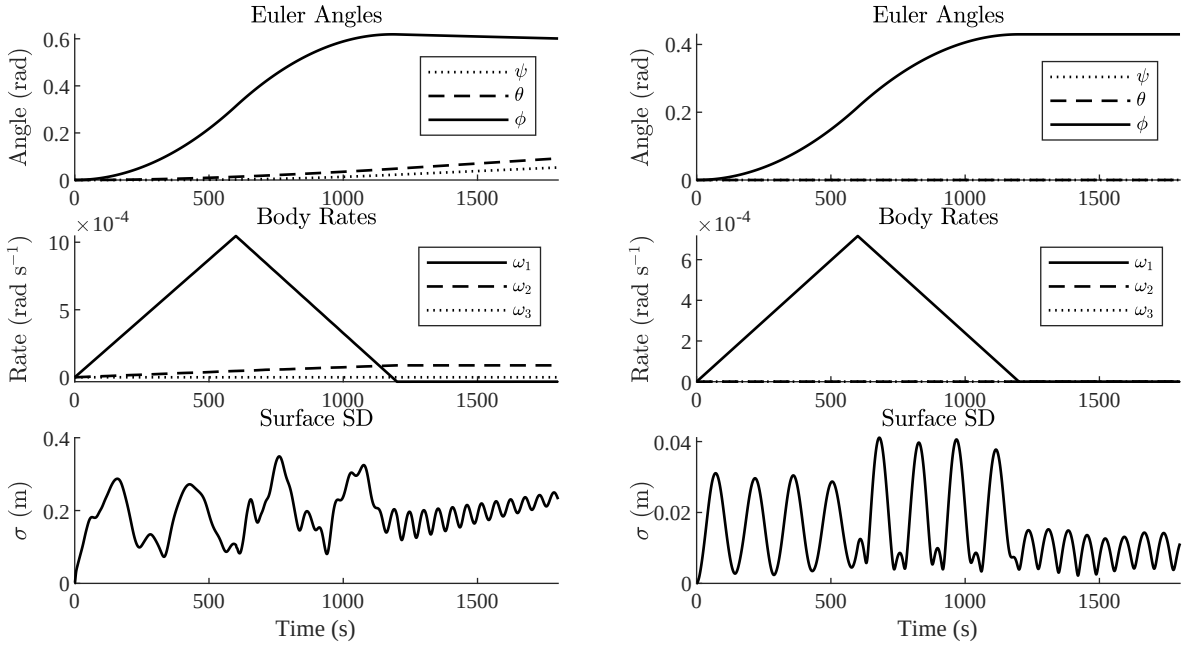

(a) Centralised torques.

(b) Distributed torques.

Figure 7: Results of simulation for Case B

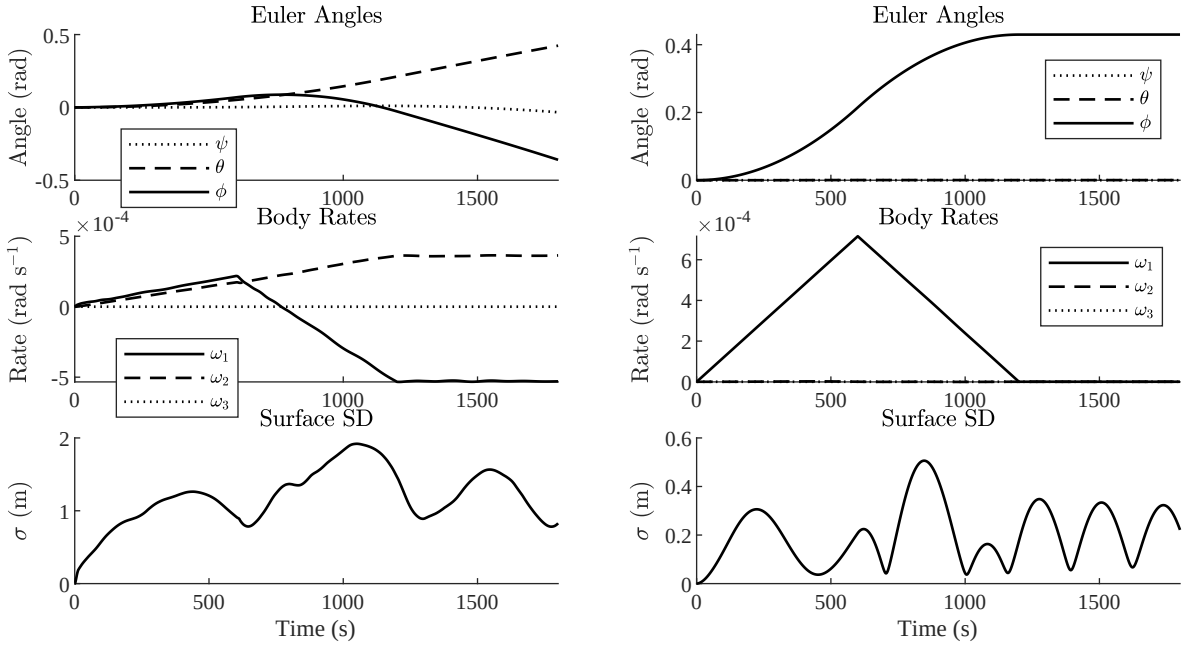

(a) Centralised torques.

(b) Distributed torques.

Figure 8: Results of simulation for Case C.

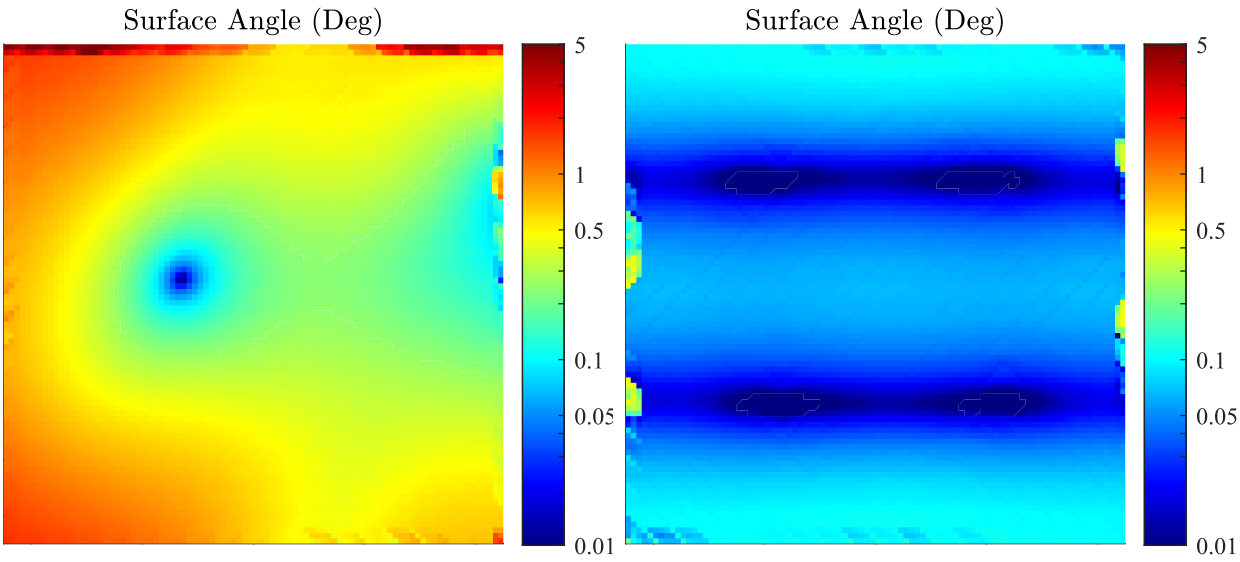

(a) Centralised torques.

(b) Distributed Torques.

Figure 9: Local surface angle at the point of maximum surface SD for Case A.

2.4. Torque-Shaping

Another approach adopted for the control of large, flexible structures is torque-shaping. Simulations are now performed to investigate the response of the structure after applying a smooth torque profile, rather than the on-off control profile considered previously. The aim of these simulations is to determine whether a smooth torque profile improves the performance of central torquing and could be an alternative to distributed actuation. Simulations of Cases A, B and C are repeated, but now with torque-shaping implemented to smooth the control signal in an attempt to reduce the magnitude of the flexible response and improve performance. Torque-shaping is well-studied for the control of spacecraft with flexible appendages, and known to reduce the impact of the flexible response on the control efficacy [48]. One torque-shaping strategy is to use the versine function (versine(θ)=1-cos(θ)) to remove discontinuities in the control signal and provide a smooth function, which has been shown to reduce jerk in attitude manoeuvres of a flexible spacecraft [49]. Simulations are repeated with the same parameters, but with a torque profile now given by:

$$
\begin{aligned}
\tau(t) &= \frac{1}{2}\left[1-\cos\left(\pi\frac{t}{t_v}\right)\right]\tau_{\max} && \text{if} \quad t \le t_v \\
\tau(t) &= \tau_{\max} && \text{if} \quad t_v < t \le t_- - t_v \\
\tau(t) &= \cos\left(\frac{\pi}{2}\cdot\frac{t_- - t_v - t}{t}\right)\tau_{\max} && \text{if} \quad t_- - t_v < t \le t_- + t_v \\
\tau(t) &= -\tau_{\max} && \text{if} \quad t_- + t_v < t \le t_0 - t_v \\
\tau(t) &= -\frac{1}{2}\left[1+\cos\left(\pi\frac{t_0 - t_v - t}{t_v}\right)\right]\tau_{\max} && \text{if} \quad t_0 - t_v < t \le t_0 \\
\tau(t) &= 0 && \text{if} \quad t > t_0
\end{aligned}
\tag{9}
$$

where $t_- = \frac{1}{3}t_{\text{end}}$ is the point at which the torque is reversed, $t_0 = \frac{2}{3}t_{\text{end}}$ is the point where the torque is switched off and t_v is the ramp-up time of the versine smoothing function, chosen as $\frac{1}{10}t_{\text{end}}$ here. The

torque profile is shown in Fig. 10, which is a versine-smoothed version of the previous bang-bang-off control signal.

Results of the simulations for Cases A, B and C with central and disributed torquing, and torque shaping implemented, are shown in Figs. 11, 12 and 13 respectively. In all cases, the overall rotational motion of the structure is very similar to the on-off control simulations, with the exception of the angular velocity profile which has now been smoothed by the torque shaping, as is to be expected. The main result here is that, even with torque shaping implemented, the centralised torquing cases still exhibit unwanted rotations around axes other than the x_1 direction. This is most evident for Case C, the most flexible structure, which fails to perform a significant rotation at all. Comparing the surface SD in all cases, there is again an order of magnitude reduction in deformation when distributed torquing is used. For Case A, torque shaping is found to greatly reduce the amplitude of oscillations of surface SD, and with distributed torquing the structure appears to deform into an equilibrium position at each stage of the simulation. This suggests that a combination of distributed torquing and torque shaping could be used for the attitude control of relatively rigid structures, where it is desired to reduce oscillations of the surface deformation. The results also show that distributed torquing could be particularly suitable for the attitude control of extremely flexible structures, represented by Case C, as although there is a large surface deformation the structure is successfully rotated around the desired axis. There is again a notable rise in SD in the last third of the simulations when central torquing is implemented, seen in Figs. 11 and 12. As noted for the previous simulations, this arises due to the initially large local deformation settling into a more uniform deformation across the structure, which has a larger surface SD despite being a lower energy configuration of the spring-mass system. The simulation shown in Fig. 11 was performed for an extended duration and the SD was seen to continue rising to a maximum value of 0.085 at 7800 s, before returning to zero due to the structural damping.

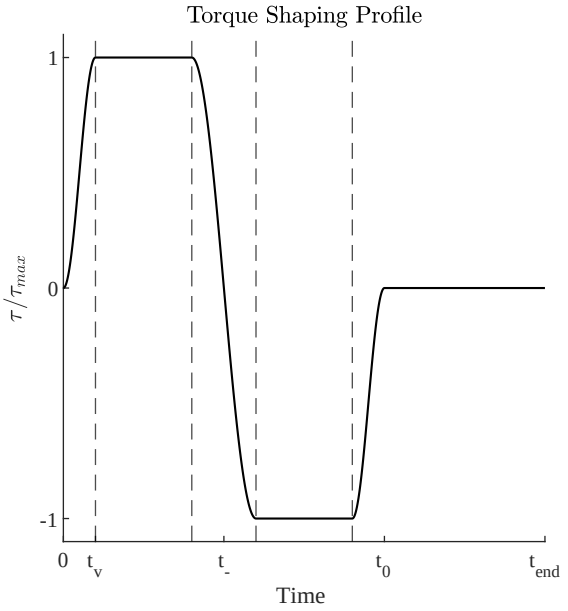

Figure 10: Versine-smoothed torque profile

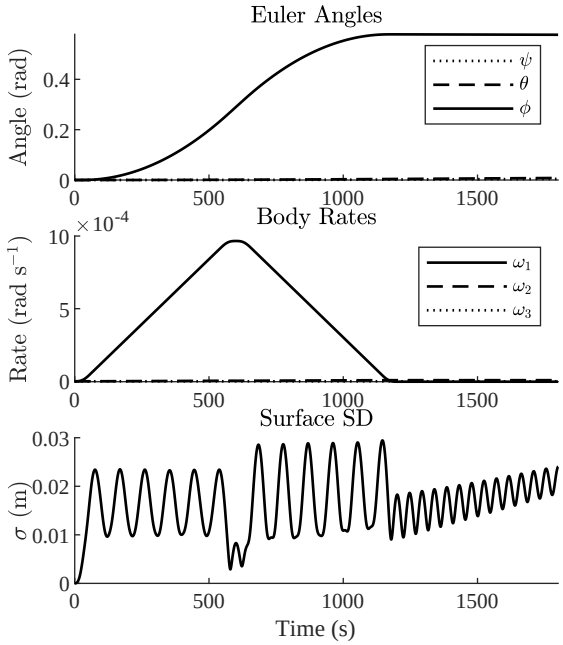

(a) Centralised torques with torque shaping.

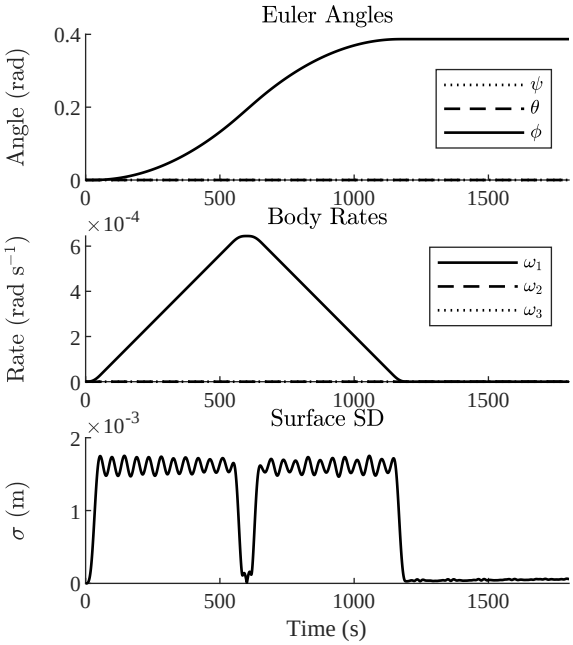

(b) Distributed torques with torque shaping.

Figure 11: Results of simulation for Case A with torque shaping implemented.

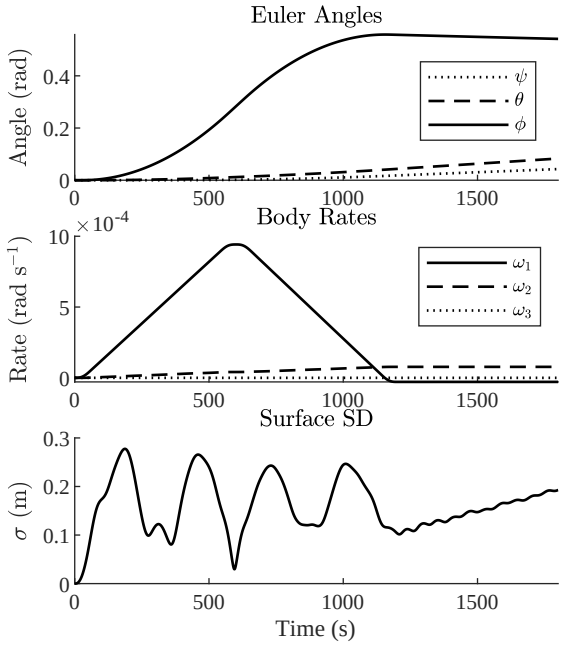

(a) Centralised torques with torque shaping.

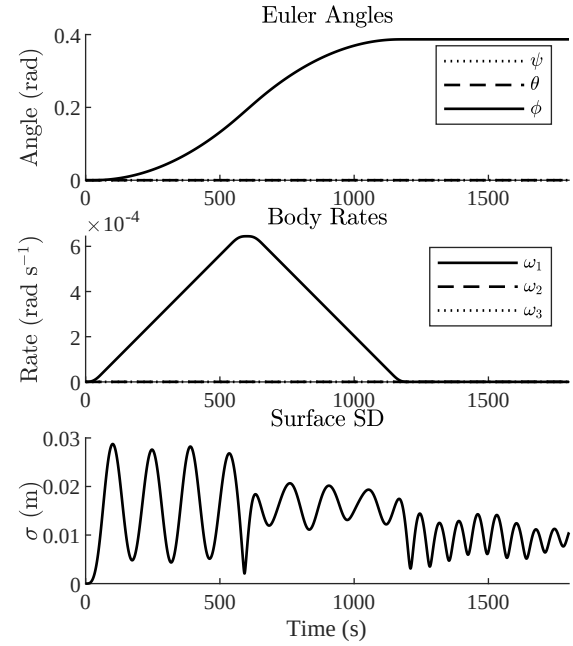

(b) Distributed torques with torque shaping.

Figure 12: Results of simulation for Case B with torque shaping implemented.

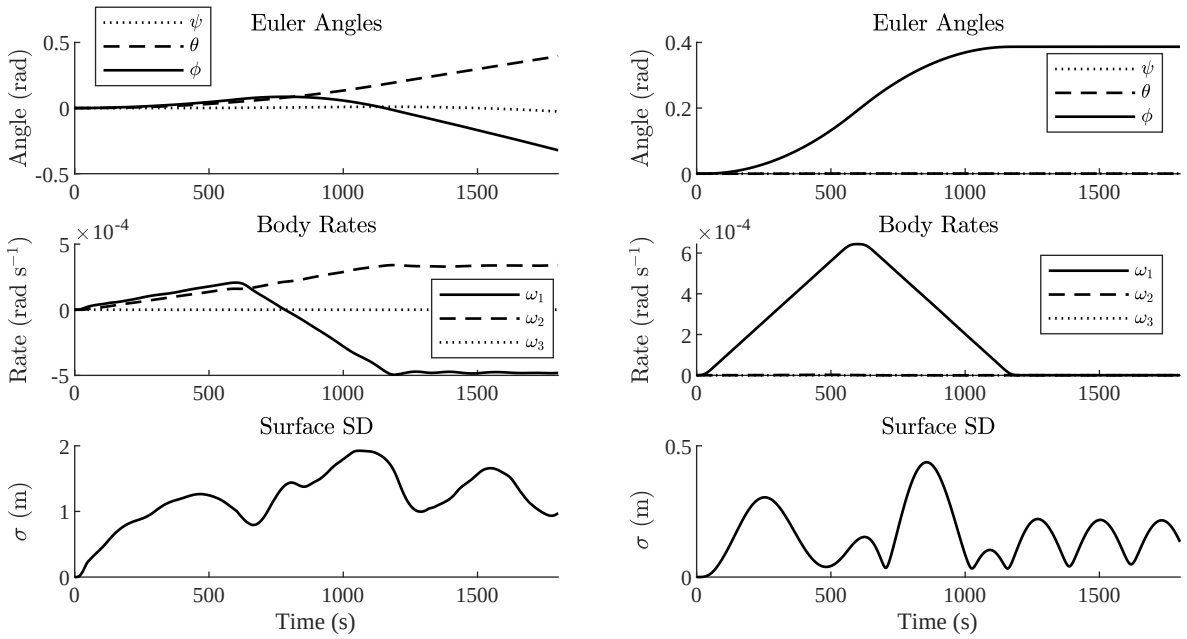

(a) Centralised torques with torque shaping.

(b) Distributed torques with torque shaping.

Figure 13: Results of simulation for Case C with torque shaping implemented.

3. Torque Distribution for Magnetorquer Arrays

To further investigate the use of distributed torques, and particularly magnetorquer arrays, for the attitude control of large space structures, a specific model of a large structure with an embedded array of magnetorquers is proposed and investigated through simulation. For these simulations, a torque distribution algorithm has been developed which approximates a continuous control signal by activating an integer number of available magnetorquers. Commonly the output of a magnetorquer is scaled by using pulse-width modulation, or bang-bang control signals are used. The algorithm developed here presents an alternative to applying pulse width modulation (PWM) to the full array of magnetorquers, where if a torque with a value lower than the maximum is desired, a fewer number of magnetorquers are activated. This strategy reduces the losses associated with the rapid switching of the magnetorquers required by PWM.

The proposed magnetorquer array consists of an $n \times n$ square grid, which has two perpendicular magnetorquers placed at each point. A magnetorquer array embedded within the spring-mass model is illustrated in Fig. 3a, where each red and blue connecting element represents a magntorquer. The magnetic dipole moments of these magnetorquers are coplanar with the structure's surface, and aligned with the body-frame x_1 and y_1 axes. Figure 14 illustrates the dipole moment directions, which are labelled $\boldsymbol{m}_{x1}$ and $\boldsymbol{m}_{y1}$, for the dipole moments in the x_1 and y_1 directions respectively. The torque produced by each dipole is found by taking the cross product with the external field $\boldsymbol{B}$, and are denoted by $\boldsymbol{\tau}_1$ and $\boldsymbol{\tau}_2$. The subscripts 1 and 2 are used to denote this and avoid implying that $\boldsymbol{\tau}_1$ and $\boldsymbol{\tau}_2$ are aligned with the x_1 and y_1 axes, as these vectors lie in the plane normal to the magnetic field. Although $\boldsymbol{m}_{x1}$ and $\boldsymbol{m}_{y1}$ are perpendicular, for an arbitrary orientation of the plane with respect to the magnetic field, $\boldsymbol{\tau}_1$ and $\boldsymbol{\tau}_2$ will not be perpendicular in general. This can be shown by taking the scalar product of the two torque vectors:

$$\begin{aligned} \boldsymbol{\tau}_1 \cdot \boldsymbol{\tau}_2 &= (\boldsymbol{m}_{x1} \times \boldsymbol{B}) \cdot (\boldsymbol{m}_{y1} \times \boldsymbol{B}) \\ &= (\boldsymbol{m}_{x1} \cdot \boldsymbol{m}_{y1})(\boldsymbol{B} \cdot \boldsymbol{B}) - (\boldsymbol{B} \cdot \boldsymbol{m}_{y1})(\boldsymbol{m}_{y1} \cdot \boldsymbol{B}) \\ &= -(\boldsymbol{m}_{x1} \cdot \boldsymbol{B})(\boldsymbol{m}_{y1} \cdot \boldsymbol{B}) \end{aligned} \tag{10}$$

Equation 10 vanishes only in the case when the magnetic field is perpendicular to one of the dipole directions, which shows that $\boldsymbol{\tau}_1$ and $\boldsymbol{\tau}_2$ are not generally perpendicular. As the torque vectors provided by the magnetorquers of each direction are not perpendicular in general, an expression must be found for the number of dipoles in each direction to activate in order to compose a reference torque. Figure 15 shows an example of how a reference torque may be generated using this configuration. It can be seen that, in this example, $\boldsymbol{T}_{ref}$ is closely approximated by activating two x_1 direction magnetorquers, and two y_1 direction magnetorquers. In general, the number of magnetorquers in each direction to activate can be found by decomposing an arbitrary reference torque vector into components.

The total actuation torque, $\boldsymbol{T}$, must be constructed from some integer multiples of $\boldsymbol{\tau}_1$ and $\boldsymbol{\tau}_2$, since there can only be an integer number of activated dipoles. This requirement can be written as:

$$\boldsymbol{T} = N_1\boldsymbol{\tau}_1 + N_2\boldsymbol{\tau}_2 \tag{11}$$

Then N_1 is found using the scalar product of the reference torque and $\boldsymbol{\tau}_1$, and rounding to the nearest integer, unless the value is greater than n^2. In that case, all the magnetorquers are activated and the controller is saturated. Therefore:

$$N_1 = \left\lfloor \frac{\boldsymbol{T}_{ref} \cdot \boldsymbol{\tau}_1}{|\boldsymbol{\tau}_1|^2} \right\rceil \tag{12}$$

Similarly, N_2 is given by an equivalent expression, except that N_2 is reduced by taking into account the contribution to the $\boldsymbol{\tau}_2$ direction already given by $N_1\boldsymbol{\tau}_1$, so that:

$$N_2 = \left\lfloor \frac{\boldsymbol{T}_{ref} \cdot \boldsymbol{\tau}_2 - N_1\boldsymbol{\tau}_1 \cdot \boldsymbol{\tau}_2}{|\boldsymbol{\tau}_2|^2} \right\rceil \tag{13}$$

There is now the issue of deciding which magnetorquers are to be activated on the square array. It is assumed desirable to have the activated magnetorquers as evenly distributed as possible, to make full use of the array and distribute the loads throughout the structure. The issue of selecting which actuators to activate can be considered an analogue to placing N points evenly within a square region, which is in general not a trivial problem and has been studied extensively in the field of computer science [50, 51]. If N is a square number, it is easy to visualise an even distribution where the points are placed on the vertices of a square grid, and for certain numbers the solution is given by dividing the area into hexagonal cells, known as hexagonal packing. These geometries cannot be exploited to give a solution for all N however. A common numerical solution to this problem, which is adapted for the magnetorquer allocation problem, is the use of Voronoi diagrams and *Lloyd's Algorithm*, which evenly distributes a set of points in Euclidean space within uniform cells [52].

A Voronoi diagram is a partitioning of a plane based on the distance to the nearest point of a set of specified points. Figure 16a shows the Voronoi diagram for a set of 21 random points placed in a square

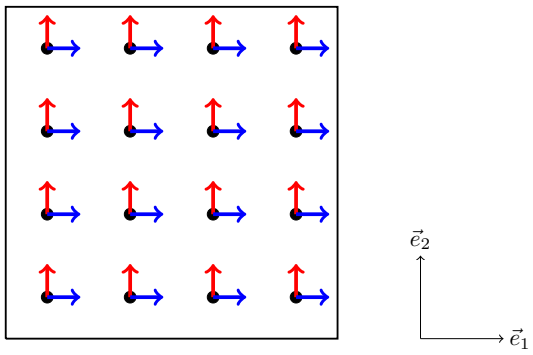

Figure 14: Square array of magnetorquers with two orthogonal dipoles at each grid point.

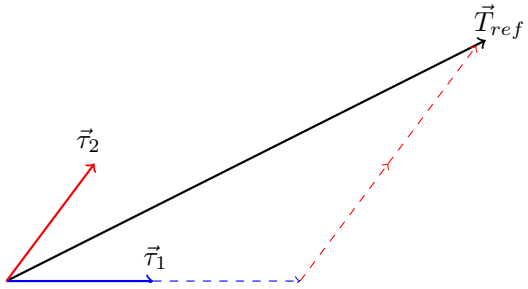

Figure 15: Example composition of torque $\boldsymbol{T}_{ref}$ from component vectors $\boldsymbol{\tau}_1$ and $\boldsymbol{\tau}_2$ for an arbitrary orientation of the array.

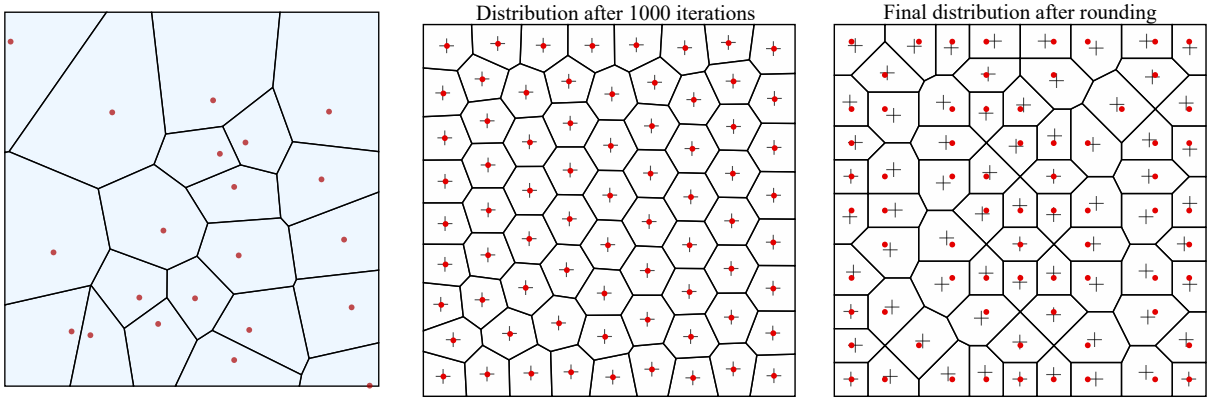

(a) Voronoi diagram for 21 points placed at random in a square region.

(b) Placing 72 points evenly on a 10×10 grid with Lloyd's algorithm. Magnetorquers located at the sites marked in red will be activated.

Figure 16: Voronoi diagram and magnetorquer selection process

region. Each cell bounds the region of space that is nearer to the contained red generator point than any other. Lloyd's algorithm generates a Voronoi diagram for a set of points, and then calculates the centroid of each cell in that diagram. The set of initial generating points is then replaced with the centroids, and a new diagram generated. This process is repeated until the change in centroid position falls below a set tolerance. This algorithm is known to converge onto a distribution known as a centroidal Voronoi tesselation, proven to be an optimal solution for a number of resource allocation problems, as the points approach an even distribution in space with cells of equal area [53].

In the context of the orthogonal dipole array described here, this approach can be used to select which magnetorquers to activate at a given time. For a given orientation, and desired torque, the number of dipoles in both possible directions that must be activated are given by Eqs. 12 and 13. For each dipole direction $i = 1, 2$, N_i random points are generated within a square region which represents the array. Lloyd's algorithm is then applied until a satisfactory distribution of points is found. As the array consists of dipoles placed at discrete points, the nearest dipole to each generated point of the final set is then selected and activated. As an example, consider a 10×10 array of orthogonal dipoles, and assume that Eq. 12 has been evaluated so that the controller must activate 72 of the 100 dipoles. The algorithm is run until the centroids do not change by more than a set tolerance, in this case resulting in 1000 iterations. The algorithm runtime was 0.25 s within MATLAB on a 2.3 GHz CPU, though it is noted that the magnetorquer activation patterns could be precomputed in practice and so the onboard runtime of the algorithm will not be an issue for future implementation. Figure 16b shows the point distribution and Voronoi diagram generated by the algorithm. The final step involves rounding the centroids to the nearest actuator point. The magnetorquers located at the sites marked in by the circular points on the right side of Fig. 16b will then be activated.

4. Orbital Simulations of a Large Space Structure with Distributed Magnetorquers

Simulations are now used to demonstrate the attitude control of a large structure using the magnetorquer array described in Sec. III, in the presence of gravity gradient torques and a changing magnetic field. First, a scaling law is developed to demonstrate how the magnetorquer array torque and gravity gradient torque scale with the structure's side length. These scaling laws lead to reasonable estimates of the structure's mass and required control torques, and are used to define the physical parameters used in the later orbital simulations. Simulations are performed to demonstrate detumbling, using the well-known Bdot control law, and two rest-to-rest manoeuvres which make use of a quaternion error feedback controller. The aims of these simulations are: 1) to show that magnetorquers can provide sufficient torques for the attitude control of a lightweight truss structure at this scale; 2) to demonstrate which axes these manoeuvres can be performed around given the geometric constraints of magnetic attitude control, and 3) to show that the

distributed array and torque distribution algorithm allows flexible structures to be controlled successfully by the application of rigid-body control laws; since torque distribution reduces structural deformation and the response to the control torques more closely resembles that of a rigid body.

4.1. Scaling of Magnetorquer Arrays

To provide an adequate degree of attitude control, the magnetorquer array must be capable of producing a torque at least as large as the gravity gradient torque that a large structure will experience on orbit. Aerodynamic and radiation pressure torques are not considered for simplicity. The gravity gradient torque scales with the moment of inertia and thus the square of the structure's length. For a rigid body this is given by: [54]

$$\boldsymbol{T}_{\text{grav}} = 3\frac{\mu}{r^5}\boldsymbol{r}_b \times \mathcal{I}\boldsymbol{r}_b \tag{14}$$

where $\boldsymbol{r}_b$ is the position vector of the centre-of-mass, expressed in body frame coordinates, and $\mathcal{I}$ is the inertia tensor. Using the inertia tensor of a thin, square plate, $\mathcal{I}_1 = \mathcal{I}_2 = 1/12Md^2$, $\mathcal{I}_3 = 1/6Md^2$, and taking the maximum value which occurs when the structure is at a 45° angle to the local vertical, Eq. 14 leads to:

$$\boldsymbol{T}_{\text{grav}}^{\max} = \frac{\mu M d^2}{8r^3} \tag{15}$$

where M is the total mass of the structure (assumed uniformly distributed), d the sidelength and r the orbital radius. As noted previously, it is assumed that the dipole moment and thus torque produced by a magnetorquer is proportional to its mass, i.e. the dipole moment produced by a given mass of magnetorquers is $M_{\text{dip}} = \kappa_\tau M_\tau$, where κ_τ is the constant of proportionality and M_τ the total mass of magnetorquers. This assumption is based on the fact that magnetic torque rods are solenoids, which produce a torque that is proportional to the number of turns in the coil. Increasing the number of turns in this solenoid then leads to a proportional increase in both mass and torque. It is also assumed that this relationship remains linear despite the magnetorquer mass being distributed between the array points. The maximum actuator torque is achieved when the dipole moment is perpendicular to the external field, and is found from Eq. 3:

$$T_{\text{ac}}^{\max} = \kappa_\tau M_\tau B \tag{16}$$

For a given scale of structure, a certain mass of magnetorquers is required to have $T_{\text{ac}} \geq T_{\text{grav}}$. The fraction of structural mass which must be allocated to magnetorquers to meet this condition is found by equating Eqs. 15 and 16, and substituting $M_\tau = \lambda_f M$, where λ_f is the fraction of total mass allocated to magnetorquers. B is approximated as a dipole field for this analysis, given by $|B| = B_0\left(\frac{R_E}{r}\right)^3$ where $R_E = 6370$ km is the radius of the Earth and B_0=3.12×10^{-5} T is the average field strength at the surface of the Earth. These substitutions lead to an expression for λ_f, the fraction of total structural mass that must be allocated to magnetorquers in order to have an achievable actuator torque equal to the maximum gravity gradient torque:

$$\lambda_f = \frac{\mu d^2}{8B_0 R_E^3 \kappa_\tau} \tag{17}$$

Equation 17 has no r dependence, since both the gravity gradient and dipole field strength fall with r^3. However, although the torques are equal the magnetic torque magnitude available for active control falls with increasing orbit radius. Equation 17 shows that the required magnetorquer mass fraction scales with d^2, suggesting the scale of structures for which distributed magnetorquer arrays would be suitable is limited, and scales inversely to κ_τ, the dipole moment to mass ratio of the magnetorquers used. As mentioned in Sec. 2.2, magnetorquers are available commercially with κ_τ =100 Am^2 [46], though this is a larger value than the majority of magnetorquers with flight heritage, which are found to have κ_τ on the order of 10 Am^2/kg, [55]. The range in values here is thought to be due to the fact that many of these torquers were flown in CubeSats, their dipole moment is most likely limited by available power or thermal constraints. For the type of large structure considered here, a considerable quantity of solar radiation can be intercepted and so power will not likely be a limiting factor, and so the larger value of κ_τ =100 Am^2 is thought reasonable,

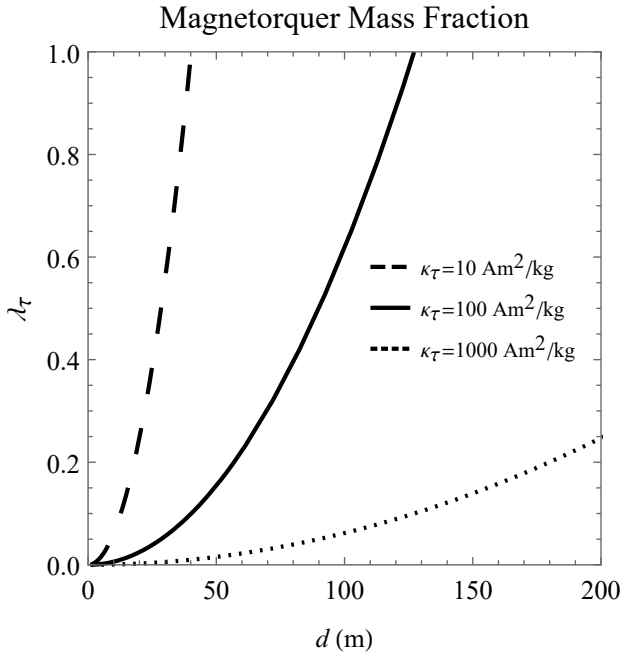

Figure 17: Required magnetorquer mass fraction as a function of structure sidelength for a range of dipole moment to mass ratios.

though it is possible that even higher values of κ_τ could be achieved. Figure 17 shows λ_τ against d for a range of κ_τ, demonstrating the maximum scale of structure for which distributed magnetorquer arrays with a given κ_τ would be suitable. For $\kappa_\tau = 100$ Am^2/kg, the figure suggests a side length of 100 m could be controlled, assuming it were reasonable to allocate up to 60% of the total structural mass for the attitude control system. It is also notable that the total mass doesn't appear in Eq. 17, although more massive structures will experience smaller angular accelerations. In Sec. A.1 it was found that distributed torquing allowed the control of more flexible structures than central torquing. More flexible structures will have a lower mass, and so although a 100 m structure would require a minimum of 60% of its mass to be magnetorquers, the structure itself can be much less massive than would be necessary to provide the required bending stiffness for centralised torquing. This analysis suggests that distributed magnetorquer arrays are particularly suitable for lightweight, flexible structures, at length scales up to approximately 100 m for currently available magnetorquers.

4.2. Detumbling with a Bdot Control Law

The Bdot control law is commonly used to allow angular momentum dumping through magnetorquers. This control law is considered here as it is so commonly used, and because angular momentum dumping is often the primary use of magnetic torque rods in conventional spacecraft. The algorithm provides an expression for the desired control torque, $\boldsymbol{T}_{Bdot}$, in terms of the body rates, $\boldsymbol{\omega}$, of the spacecraft and the magnetic field, $\boldsymbol{B}$, [56], such that:

$$\boldsymbol{T}_{Bdot} = k_{\text{Bdot}}(\boldsymbol{\omega} \times \boldsymbol{B}) \times \boldsymbol{B} \tag{18}$$

where k_{Bdot} is the controller gain. Although we are considering a flexible body, we again use the best fitting rotation matrix of the nodal points to describe the structure's attitude, and estimate the angular rates at each time step using the backward difference formula. This treats the structure as a rigid-body for the controller, and so it is assumed to only be effective should the structure maintain its initial shape sufficiently. The structure is placed on a polar, circular orbit with altitude 800km and so air drag is assumed

to be negligible. Moreover, radiation pressure will also be neglected in order to assess the use of magnetic attitude control. The magnetic field is calculated at each time step using the World Magnetic Model (WMM) for 2020 [57]. Although there will be slight variation in the magnetic field over the structure itself, this variation is negligible compared to the variation over the orbit, and so for computational efficiency the magnetic field is only calculated at the centre-of-mass of the structure and is assumed constant across its span.

Considering the scaling law Eq. 17, a 75×75 m square structure is selected for the following simulations. The magnetorquers are assumed to have κ_τ of 100 $\mathrm{Am}^2/\mathrm{kg}$, and so a side length of 75 m means that a magnetorquer mass fraction of 50% would provide an actuator torque greater than the gravity gradient torque, illustrated in Fig. 17. The structure's mass is set to 200 kg, 100 kg of which is allocated to magnetorquers while another 100 kg is the structural mass. This structural mass is assumed to provide a bending stiffness of 10^3 Nm^2, the same as Case A in Sec. II, based on the fact that areal densities on the order of 10 $\mathrm{g/m}^2$ are capable of achieving this level of rigidity for solar sails. The spring constant used in the model is then determined as in Sec. II. The 100 kg of magnetorquers are capable of producing a total dipole moment of 10000 Am^2, which is distributed between 380 magnetorquer sites along both the x_1 and y_1 body axis directions, as illustrated in Fig. 2a) but here with 20×20 cube units. All other simulation parameters are the same as the previous simulations, given in Table 1. The initial angular velocity is set to $\boldsymbol{\omega}_0 = (0.01, 0.007, 0)$ rad s^{-1}. While this is a modest rate for a conventional satellite, it represents a significant angular velocity for a 75 m structure. Through simulation it was found that the structure failed through buckling at larger angular velocities due to centripetal forces. This was observed for angular velocities approximately an order of magnitude larger than ω_0, so the initial angular velocity selected is then assumed to be a rate at which a structure of this scale could be considered tumbling but not at danger of structural failure. The magnitude of ω_0 is also around three times as large as the maximum angular velocity reached during the simulation in Fig. 6. It is also an order of magnitude larger than the orbital angular velocity. Structural parameters and other simulation data is summarised in Table 2

Structural Parameters		
Length	d	75 m
Magnetorquer dip. to mass ratio	κ_τ	100 $\mathrm{Am}^2/\mathrm{kg}$
Magnetorquer mass fraction	λ_f	50%
Total Mass	M	200 kg
Bending stiffness	EI	10^3 Nm^2
Structural units		20×20
Total number of torquers for each direction		380
Total number of particles		800
Orbital altitude	R	800 km
Detumbling		
Initial ang. velocity	$\boldsymbol{\omega}_0$	(0.01,0.07,0)
Bdot controller gain	k_{Bdot}	1×10^{12}
Simulation runtime	t_{end}	2.5 hours
Slew Manoeuvres		
Proportional Gains	$\mathcal{P}_q$	(10,50,1)
Derivative Gains	$\mathcal{P}_\omega$	(1600,8000,800)
Simulation runtime	t_{end}	4.2 hours
Simulation timestep	dt	0.1 s
Integration method	Runge-kutta 4th order	
Magnetic Field	World Magnetic Model (2020)	

Table 2: Parameters used for orbital simulations.

The results of the simulation are shown in Fig. 18. The structure is seen to detumble to a state with all rates below 1×10^{-3} rad s^{-1}, or 10% of the original rates, in 1 hour. At this point there is some fluctuation

in the body rates, presumably due to the influence of the gravity gradient torque, but the controller corrects these disturbances and the body rates remain close to zero. Figure 19 shows the control profile during the simulation, which indicates the number of magnetorquers activated at a given time and their polarity. During the first hour of detumbling the controller is saturated, with nearly all magnetorquers activated. Later, once the majority of angular momentum has been removed, fewer magnetorquers are activated, although there is

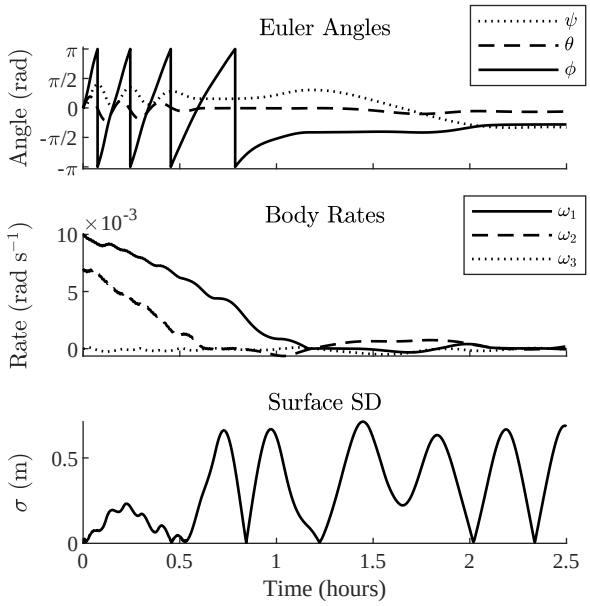

Figure 18: Detumbling of a structure with distributed torques.

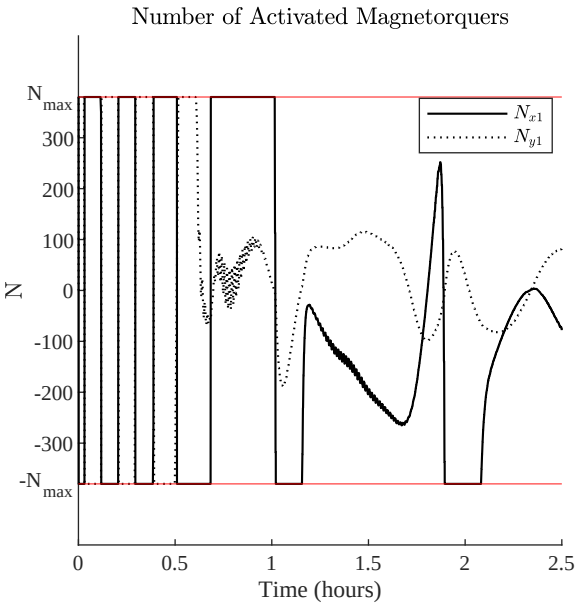

Figure 19: Control signal during detumbling.

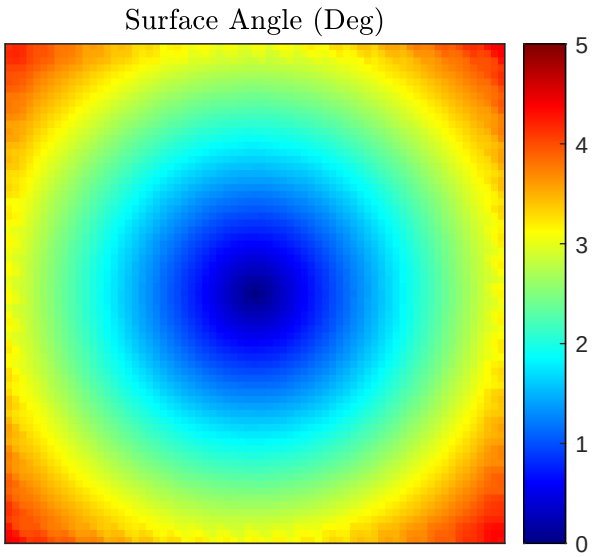

Figure 20: Local surface angle at point of maximum surface SD during detumbling.

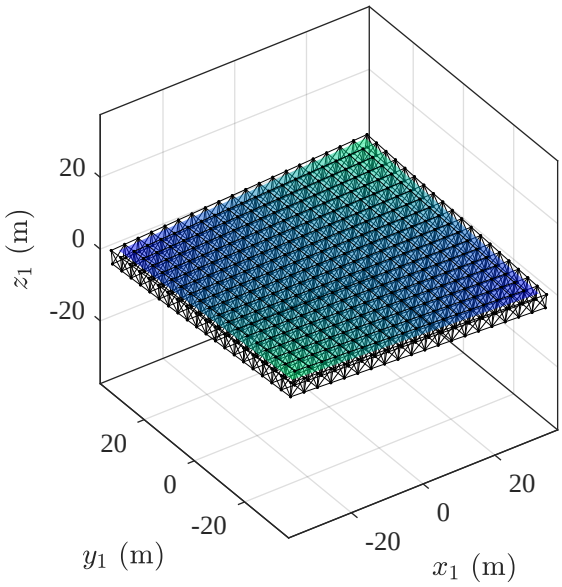

Figure 21: Structural deformation at point of maximum surface SD.

another point of saturation at approximately 2 hours. This is due to the coincidence of a point of maximum gravity gradient torque with minimum control effectiveness, which occurs when the field is oriented within the plane of the structure. The surface is seen to experience large deformations while detumbling, with the surface standard deviation reaching a maximum value of 0.5 m. As the surface deviation is oscillating regularly it is likely some normal modes have been excited, which could be caused by the actuator torques changing periodically while the structure rotates, or by the difference in magnitude of the gravitational forces acting upon the lumped masses of the structure. The surface deformation is shown in Figs. 20 and 21, which shows the local surface angle and shape of the structure at the point of maximum surface SD. The edges of the surface make an angle of 4° to the average plane, and the structure is visibly twisted in Fig. 21. The allowable deformation would depend on the specific structure and a limit on this is not considered here, but again it is noted that the deformation is smooth with no points of high curvature that may cause buckling.

4.3. Slew Manoeuvres with Quaternion Error Feedback Control

In addition to angular momentum dumping, magnetorquers can also be used directly for manoeuvring, although the geometric constraint of being unable to generate a torque in the external field direction leads to an underactuated control problem for general re-orientations. Despite these disadvantages, some limited attitude control is still possible, depending on the orbit selected, and here we investigate the capabilities of the distributed magnetorquer array for performing slew manoeuvres. The aim of these simulations is to demonstrate which manoeuvres can be achieved when the proposed array geometry is placed in a polar orbit, and how effective the distributed array is at enacting these manoeuvres.

A quaternion error feedback controller is used to generate a reference torque for performing these manoeuvres. Again, this controller is primarily used for rigid-body rotations, and it is applied to the flexible structure by considering the best-fitting rotation for the set of nodal positions. An error quaternion q_{err} is defined using the quaternion product of the desired orientation quaternion, q_{ref}, with the current orientation conjugate, q_t^* [54], such that:

$$q_{err} = \boldsymbol{q}_{ref}\boldsymbol{q}_t^* \tag{19}$$

The vector part of this pure quaternion then gives the direction of the torque required to achieve the desired orientation. A reference torque can be built from this vector along with a damping term proportional to the current angular velocity vector, such that:

$$\boldsymbol{T}_{ref} = -P_q\boldsymbol{q}_{\text{err}} - P_\omega\boldsymbol{\omega} \tag{20}$$

where $\boldsymbol{q}_{err}$ is the vector part of the q_{err} quaternion. The ratio of the two proportional gains, P_q and P_ω, can be adjusted to change the characteristics of the controller, while both are scaled to generate reference torques with a magnitude achievable by the magnetorquer array.

The controller is modified to take into account the gravity gradient torque. Equation 14 is for the torque on a rigid body, where the inertia matrix is found by integrating over the body's volume. For the spring-mass structure this is therefore an estimation, but is assumed accurate so long as the original shape is sufficiently maintained. The inertia tensor is taken to be the initial mass-moments-of-inertia of the particle distribution around the principal axes, which is found by summation over the point masses. The diagonal components of $\mathcal{I}$ are given by:

$$\begin{aligned}
\mathcal{I}_1 &= \sum_i m_p(y_{1i}^2 + z_{1i}^2) \\
\mathcal{I}_2 &= \sum_i m_p(x_{1i}^2 + z_{1i}^2) \\
\mathcal{I}_3 &= \sum_i m_p(x_{1i}^2 + y_{1i}^2)
\end{aligned} \tag{21}$$

where x_{1i} is the x_1 component of the ith particle in the body frame, and likewise for y_{1i} and z_{1i}. For the 200 kg structure these components are $\mathcal{I}_1 = \mathcal{I}_2 = 1893$ kg m^2 and $\mathcal{I}_3 = 2867$ kg m^2. The reference torque

in Eq. 20 is modified to give:

$$\boldsymbol{T}_{ref} = -P_q \boldsymbol{q}_{\text{err}} - P_\omega \boldsymbol{\omega} - 3\frac{\mu}{r^5}\boldsymbol{r}_b \times \mathcal{I}\boldsymbol{r}_b \tag{22}$$

assuring the controller will now compensate for the estimated gravity gradient torque. When selecting the control gains, it was found that replacing the proportional and derivative gains P_q and P_ω with diagonal matrices $\mathcal{P}_q$ and $\mathcal{P}_\omega$ resulted in better performance. This can be understood intuitively as applying a different gain to each axis of rotation. It was found that disturbances in the angle of rotation around the z and y axis were more likely to lead to tumbling of the structure, so a larger gain is selected for the corresponding entry the gain matrices. This results in the controller prioritising the correction of any disturbances in these directions and thus reduces the risk of the structure beginning to tumble. The feedback gains are selected as $(10, 50, 1)$ and $(1600, 8000, 800)$, for the diagonal entries of $\mathcal{P}_q$ and $\mathcal{P}_\omega$ respectively.

The attempted manoeuvres are illustrated in Fig. 22. The structure is again placed in a polar orbit. As the structure orbits, the magnetic field direction is primarily in the yz-plane, and rotates around the x-axis. There is always a slight x-component to the field because it not an ideal dipole field. Additionally, because magnetic north and true north are not aligned, this variation in this component changes over multiple orbits due to the Earth's rotation, which is taken into account when calculating the field components from the WMM. The selected manoeuvres are chosen to demonstrate rotation around all three inertial axes, (I,III and IV), and to demonstrate the ability of the system to either work against the gravity gradient torque (I) or to move between gravity-gradient stable configurations (II). Simulation parameters are summarised

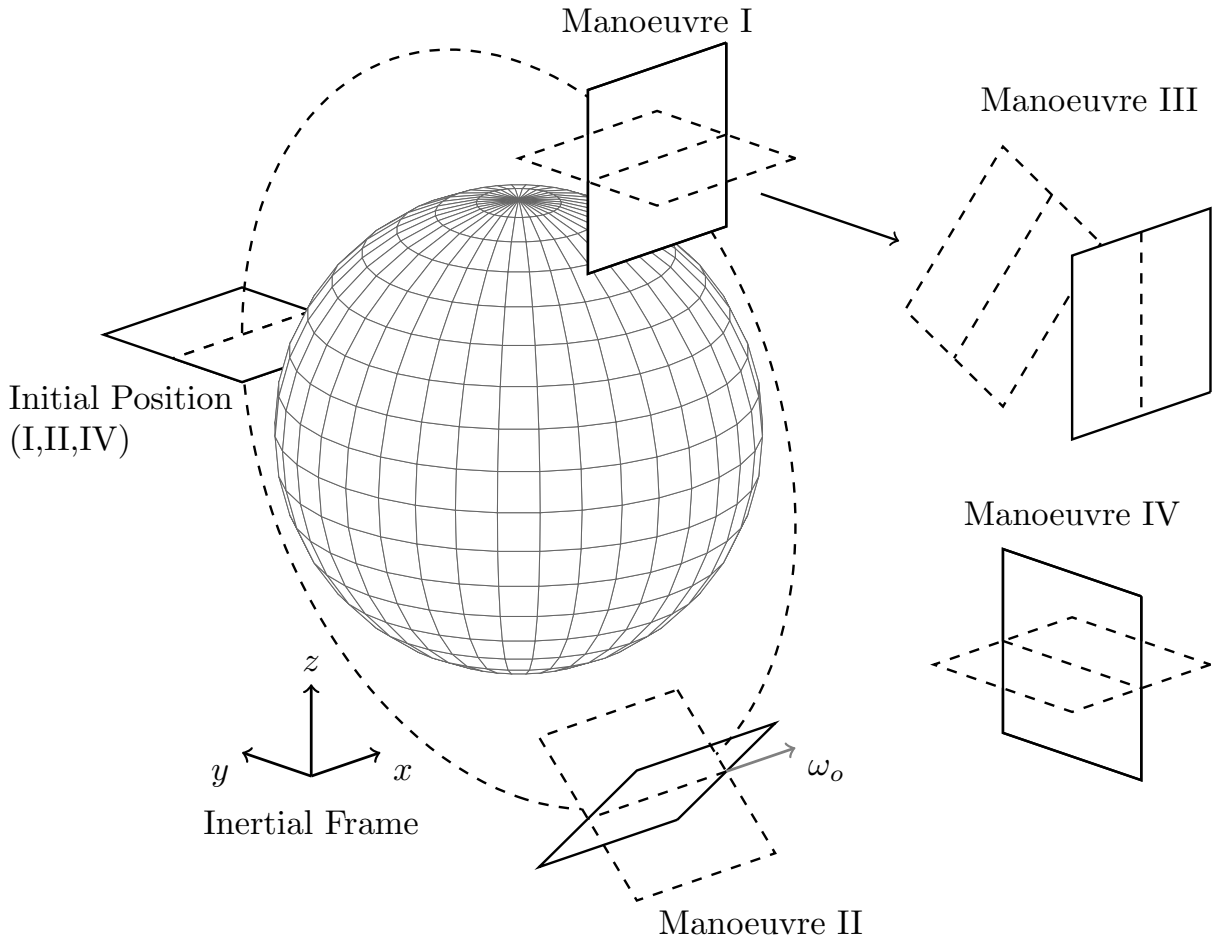

Figure 22: Illustration of Manoeuvres I-IV.

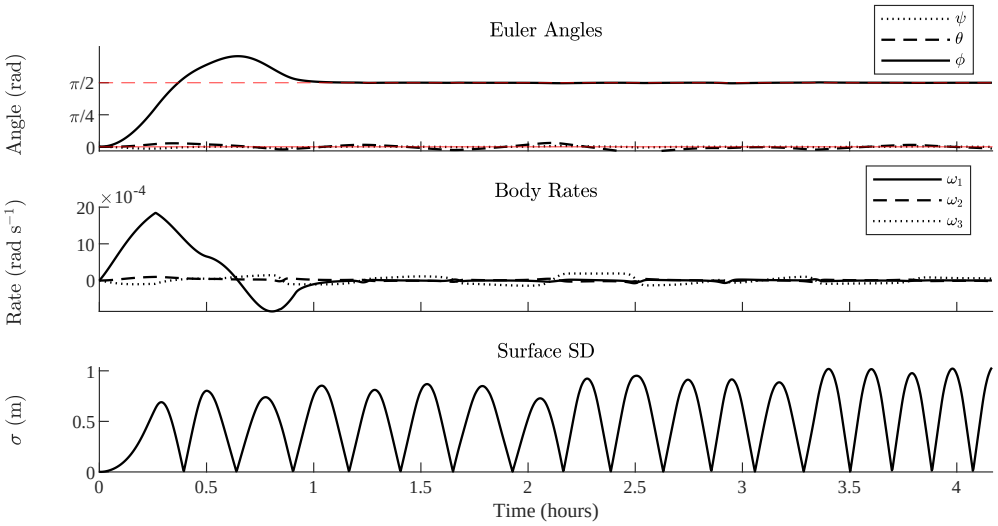

a)

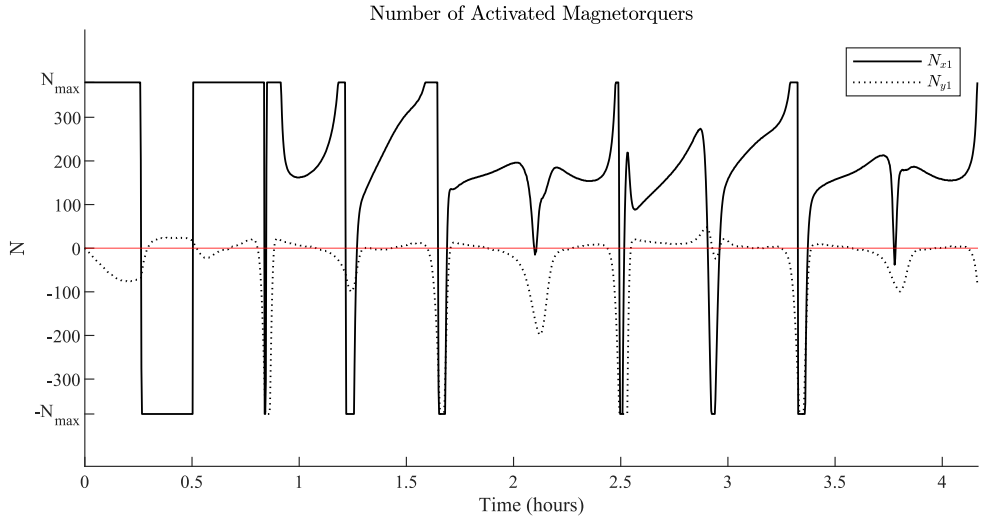

b)

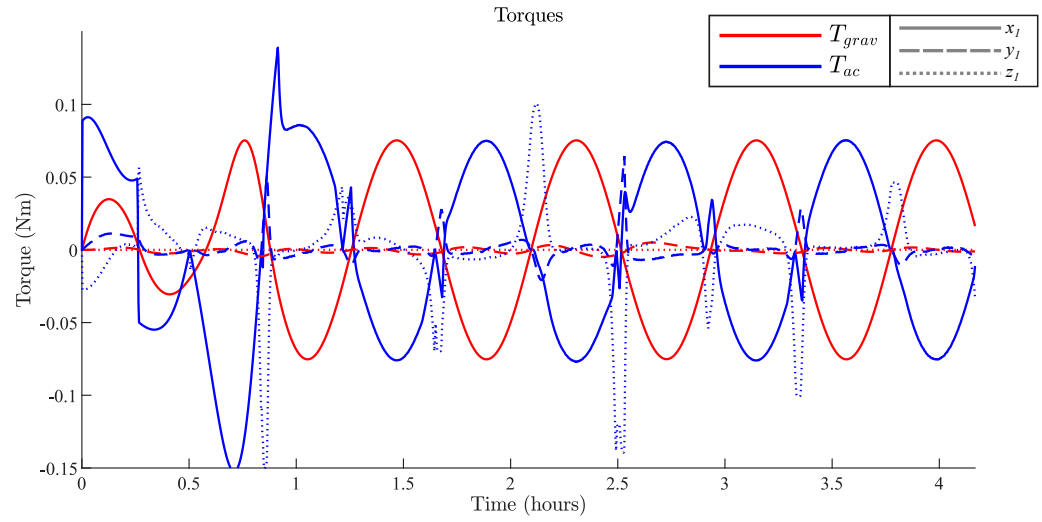

c)

Figure 23: Results of simulation for Manoeuvre I.

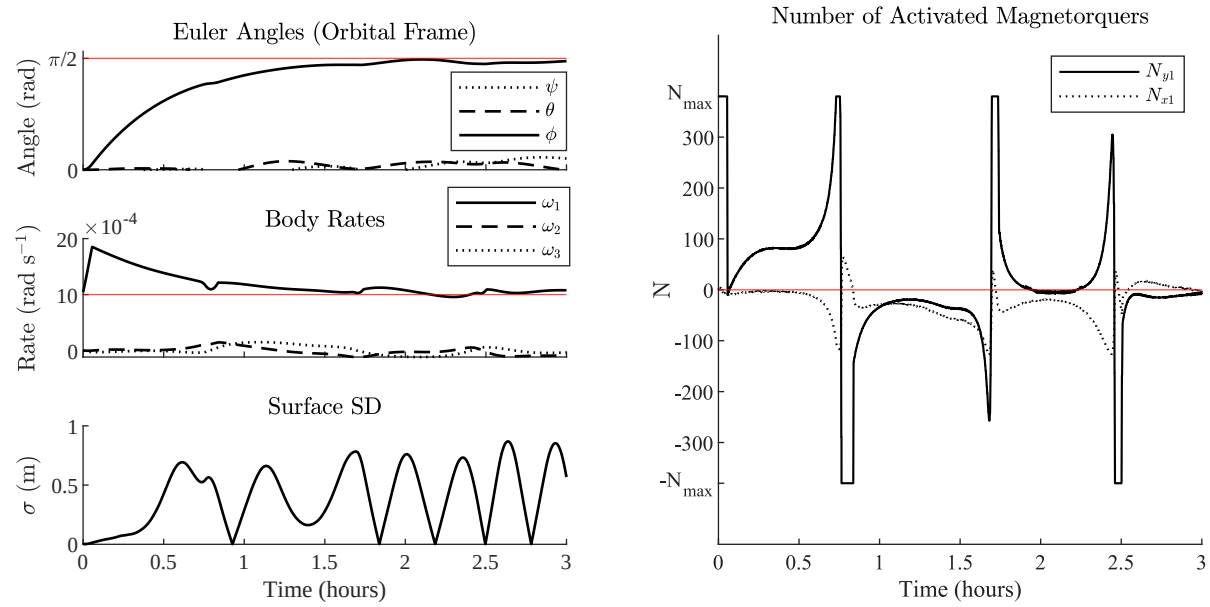

(a) (b)

Figure 24: Results of simulation for Manoeuvre II.

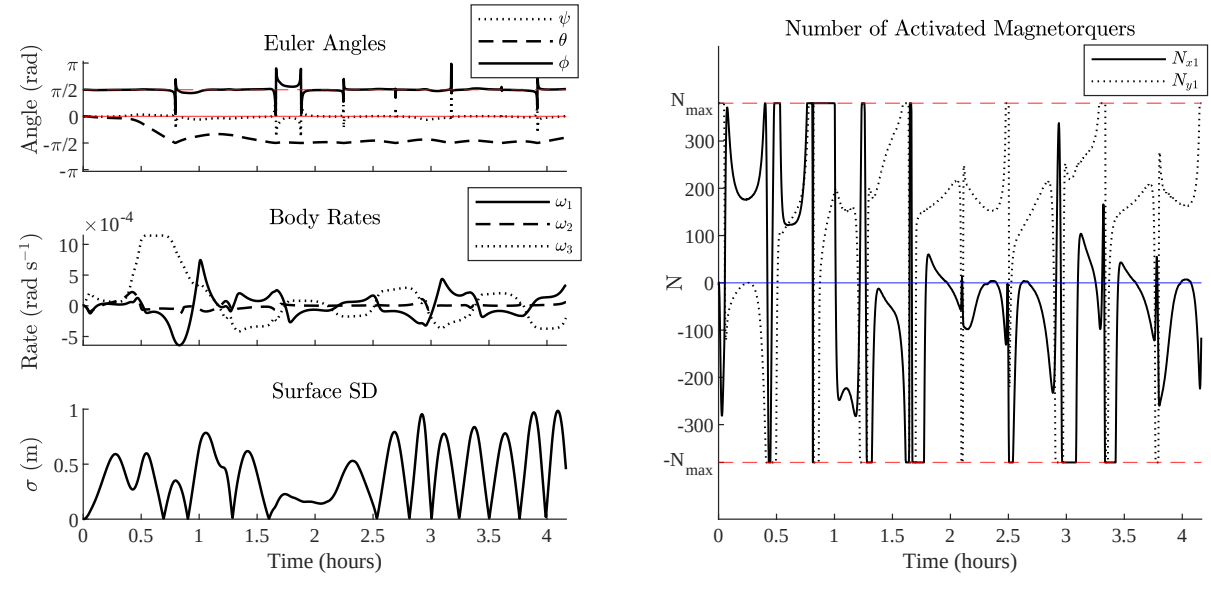

(a) (b)

Figure 25: Results of simulation for Manoeuvre III.

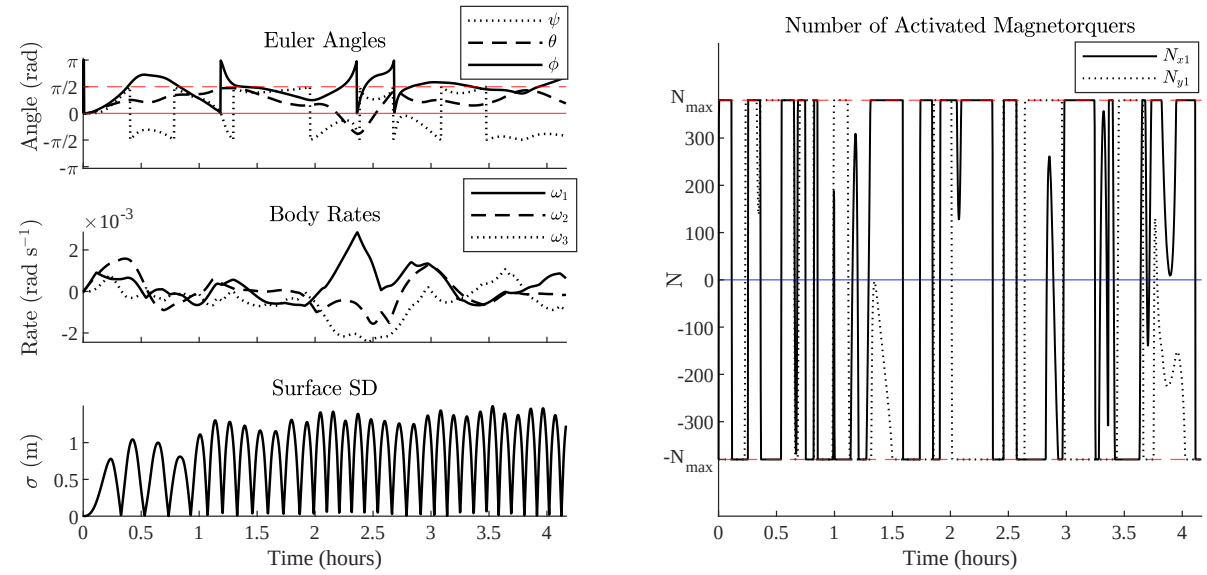

(a) (b)

Figure 26: Results of simulation for Manoeuvre IV.

in Table 2.

Results of the simulations are shown in Figs. 23 -26b, where all manoeuvres are performed successfully within approximately 1.5 hours, with the exception of Manoeuvre IV. In the case of Manoeuvre IV the desired attitude is not achieved and the structure begins to tumble. This is because when attempting to rotate around the inertial y-axis, the direction of the gravity gradient torque is not in a direction that can be counteracted by the magnetic torques produced by the system, and so this is a limitation imposed on the use of magnetic control in general rather than our control strategy. Figure 23c shows the torques experienced by the structure during Manoeuvre I, with the gravity gradient and control torques shown in red and blue respectively, and dashing used to indicate the body axis components of each. The torques are primarily around the body x_1 axis, as the desired axis of rotation, and the results show that the controller successfully counteracts this component of the gravity gradient torque over the simulation runtime of four hours. There are points at which the controller is unable to produce the required torque, due to the relative orientation of the external field and the structure, which are shown in this figure as points where T_{ac} falls to zero briefly. Notably this occurs at 0.5 hours for a significant period, when the structure is still performing the manoeuvre. The result of this period of control ineffectiveness is the structure overshooting the desired angle of $\pi/2$ rad, as shown in a). This overshooting is not underdamping caused by the gain selection, rather it is due to the coincidence of a point of large gravity gradient torque with a point of minimum control effectiveness, a scenario which may be typical of this control strategy and may need to be taken into account when planning manoeuvres. Manoeuvre II was performed to investigate the controller performance when moving between gravity gradient stabilised configurations, as opposed to working against the gravity gradient torque. As illustrated in Fig. 24b), the control effort is greatly reduced when compared to the results of Manoeuvre I. This shows that the use of gravity gradient stabilised configurations as "resting points" in between attitude manoeuvres could be an efficient strategy, depending on the mission requirements and desired attitudes. Manoeuvre III begins with the structure facing the inertial y-direction because with the initial orientation used for the other manoeuvres, as shown in Fig. 22, the magnetic torques are unable to cause rotation around the inertial z-axis. This is because the field direction is near to the positive or negative z direction for the majority of the time. However, manoeuvres I and III could be combined, in the sequence I, III and then the reverse of I, to achieve a rotation equivalent to purely rotating around the inertial z-axis. A final note is that the surface SD is much higher in all cases here than in the previous results of Sec. II,

approaching 1 m for the successful manoeuvres. This is due to the gravity gradient torque acting on the structure, as it was found that performing manoeuvres in the absence of this torque did not produce such large surface deformations. Although the surface SD is much higher here, the deformation itself is smooth with no points of large local curvature, as would be the result of using centralised torquing.

5. Conclusion

Simulation has demonstrated that distributed torques are in principle more effective at rotating a large, flexible structure than centralised torques, even when the increase in inertia of the distributed actuators is taken into account. This was demonstrated for 100 m structures with different parameters which cover a range of structural stiffnesses representative of large space structures of this scale. Of three cases considered, distributed torques are found to be more effective at inducing rotation than an equivalent torque applied to the centre-of-mass only. In addition to being able to achieve rotations, distributed torques result in lower deformation of the structure's surface, which may be desirable for many applications of large space structures.

Given that distributed torquing was found to be a desirable control strategy, magnetorquers in particular were then considered as a potential actuator. A configuration of magnetorquers was proposed for the control of a large planar structure, and a torque distribution algorithm developed which allows the overall control torque to be scaled by activating patterns of magnetorquers in the array. It was found that a large, 75 m flexible structure may be controlled by an array of magnetorquers through the application of this torque distribution algorithm, and rigid-body control laws. Both detumbling and slew manoeuvres were demonstrated through simulation, using the magnetorquer array in the presence of gravity gradient torques and a changing magnetic field. The application of these rigid-body control laws is only possible due to the torque being distributed across the structure sufficiently to approximate a rigid body, as was demonstrated in Sec. II. Slew manoeuvres were selected to demonstrate the range of possible rotations that can be enacted by the system, and it was found that rotations around the inertial x and z axes are possible for a square structure placed in polar orbit, but that due to the relative directions of the external field and gravity gradient, rotations around the inertial y-axis are not possible.

Despite the limitations of magnetic attitude control, an array of magnetorquers is attractive as they could be easily integrated into the on-orbit fabrication of a large space structure. For large space structures fabricated on-orbit, the system proposed here could provide a basic level of attitude control and stability, where the majority of the control effort is generated by the distributed magnetorquers. This could then be augmented by further actuation to suit specific mission requirements such as shape control and pointing accuracy.

6. Acknowledgements

This work was supported by the Royal Academy of Engineering under the Chair in Emerging Technologies scheme. CM was also supported by a Royal Society Wolfson Research Merit Award

References

[1] D. Beasley, Large area membrane apertures for space applications, fabrication and mechanical testing, 4th AIAA Spacecraft Structures Conference (AIAA, Grapevine, TX, 2017) 2 – 9doi:10.2514/6.2017-0853.

[2] L. Datashvili, H. Baier, E. Wehrle, T. Kuhn, J. Hoffmann, Large shell-membrane space reflectors, in: 51st AIAA/ASME/ASCE/AHS/ASC Structures, Structural Dynamics, and Materials Conference, AIAA, Orlando, FL, 2010, pp. 1 – 8. doi:10.2514/6.2010-2504.

[3] M. MacDonald, C. McInnes, Solar sail science mission applications and advancement, Advances in Space Research 48 (11) (2011) 1702 – 1716. doi:10.1016/j.asr.2011.03.018.

[4] B. Levedahl, R. P. Hoyt, T. Silagy, J. Gorges, N. Britton, J. Slostad, Trusselator™ technology for in-situ fabrication of solar array support structures, 2018 AIAA Spacecraft Structures Conference (AIAA, Kissimmee, FL, 2018). doi:10.2514/6.2018-2203.

[5] R. P. Hoyt, Spiderfab: an architecture for self-fabricating space systems, AIAA SPACE 2013 Conference and Exposition (AIAA, San Diego, CA, 2013) 1 – 17doi:10.2514/6.2013-5509.

[6] B. Jenett, K. Cheung, Bill-e: Robotic platform for locomotion and manipulation of lightweight space structures, in: 25th AIAA/AHS Adaptive Structures Conference, AIAA, Grapevine, Texas, 2017. doi:10.2514/6.2017-1876.
[7] M. Mcrobb, B. Robb, S. Ridley, C. Mcinnes, Emerging Space Technologies: Macro-scale On-orbit Manufacturing, 17th Reinventing Space Conference (British Interplanetary Society, Belfast, Northern Ireland, 2019).
[8] B. Robb, M. McRobb, C. McInnes, Magnetic attitude control of gossamer spacecraft using a 3d-printed, electrically conducting support structure, in: AIAA Scitech 2020 Forum, AIAA, Orlando, Fl, 2020. arXiv:https://arc.aiaa.org/doi/pdf/10.2514/6.2020-0714, doi:10.2514/6.2020-0714.
[9] J. C. Mankins, N. Kaya, Space solar power, the first international assessment of space solar power: Opportunities, issues and potential pathways forward (International Academy of Astronautics, August 2011).
[10] J. C. Mankins, A fresh look at space solar power: New architectures, concepts and technologies, Acta Astronautica 41 (4) (1997) 347 – 359. doi:10.1016/S0094-5765(98)00075-7.
[11] J. C. Mankins, New directions for space solar power, Acta Astronautica 65 (1) (2009) 146 – 156. doi:10.1016/j.actaastro.2009.01.032.
[12] C. Carrington, H. Feingold, Space solar power concepts: Demonstrations to pilot plants, in: 53rd International Astronautical Congress, International Astronautical Federation, Houston, TX, 2002.
[13] K. W. Billman, W. P. Gillbreath, S. W. Bowen, Introductory assessment of orbiting reflectors for terrestrial power generation (NASA-TM-73230, 1977).
[14] J. E. Canady, J. L. Allen, Illumination from space with orbiting solar-reflector spacecraft (NASA-CR-2065, September 1982).
[15] N. Lior, Mirrors in the sky : Status , sustainability , and some supporting materials experiments, Renewable and Sustainable Energy Reviews 18 (February, 2013) 401–415. doi:10.1016/j.rser.2012.09.008".
[16] L. M. Fraas, Sunbeams from mirrors in dawn-dusk orbit for earth solar power fields, 9th International Conference on Concentrator Photovoltaic Systems (American Institute of Physics, Miyazaki, Japan, 2013) 234–238doi:10.1063/1.4822239.
[17] C. R. McInnes, Space-based geoengineering: Challenges and requirements, Proceedings of the Institution of Mechanical Engineers, Part C: Journal of Mechanical Engineering Science 224 (3) (2009) 571–580. doi:10.1243/09544062JMES1439.
[18] R. Bewick, J. P. Sanchez, C. R. McInnes, The feasibility of using an L 1 positioned dust cloud as a method of space-based geoengineering, Advances in Space Research 49 (7) (2012) 1212–1228. doi:10.1016/j.asr.2012.01.010.
URL http://dx.doi.org/10.1016/j.asr.2012.01.010
[19] C. R. McInnes, Planetary macro-engineering using orbiting solar reflectors, in: V. Badescu, R. B. Cathcart, R. D. Schuiling (Eds.), Macro-Engineering: A Challenge for the Future, Springer, Dordrecht, 2006, pp. 215–250.
[20] F. Bonetti, C. McInnes, Space-enhanced terrestrial solar power for equatorial regions, Journal of Spacecraft and Rockets 56 (1) (2019) 33–43. doi:10.2514/1.A34032.
URL https://doi.org/10.2514/1.A34032
[21] W. Gilbreath, K. Billman, S. Bowen, Enhanced solar energy options using earth-orbiting mirrors, in: 13th Intersociety Energy Conversion Engineering Conference, Society of Automotive Engineers, San Diego, CA, 1978, pp. 1528 – 1534.
[22] J. M. Hedgepeth, Critical requirements for the design of large space structures, in: 2nd Conference on Large Space Platforms: Toward Permanent Manned Occupancy in Space, AIAA, San Diego, CA, 1981. doi:10.2514/6.1981-443.
[23] B. Fu, G. Gede, F. O. Eke, Controllability of a square solar sail with movable membrane tips, Proceedings of the Institution of Mechanical engineers, Part G: Journal of Aerospace Engineering 231 (6) (2017) 1065–1075. doi:10.1177/0954410016647533.
[24] M. Choi, C. J. Damaren, Structural dynamics and attitude control of a solar sail using tip vanes, Journal of Spacecraft and Rockets 52 (6) (2015) 1665–1679. doi:10.2514/1.A33179.
[25] B. Wie, Solar sail attitude control and dynamics , part 2, Journal of Guidance Control and Dynamics 27 (4) (2004) 536–544. doi:10.2514/1.11133.
[26] A. Borggräfe, J. Heiligers, M. Ceriotti, C. R. McInnes, Shape control of slack space reflectors using modulated solar pressure, Proceedings of the Royal Society A: Mathematical, Physical and Engineering Sciences 471 (2179) (2015). doi:10.1098/rspa.2015.0119.
[27] A. Borggräfe, J. Heiligers, M. Ceriotti, C. R. McInnes, Attitude control of large gossamer spacecraft using surface reflectivity modulation, in: 65th International Astronautical Congress, International Astronautical Federation, Toronta, Canada, 2014, pp. 1753 – 1759. doi:10.1016/j.buildenv.2006.10.027.
[28] J. Mu, S. Gong, J. Li, Coupled control of reflectivity modulated solar sail for geosail formation flying, Journal of Guidance, Control, and Dynamics 38 (4) (2015) 740 – 751. doi:10.2514/1.G000117.
[29] P. HUGHES, Dynamics of gyro-elastic continua, in: 24th Structures, Structural Dynamics and Materials Conference, 1983. doi:10.2514/6.1983-826.
URL http://arc.aiaa.org/doi/10.2514/6.1983-826
[30] S. A. Chee, C. J. Damaren, Optimal Gyricity Distribution for Space Structure Vibration Control, Journal of Guidance, Control, and Dynamics 38 (7) (2015) 1218–1228. doi:10.2514/1.G000293.
URL http://arc.aiaa.org/doi/10.2514/1.G000293
[31] Q. Hu, Y. Jia, S. Xu, Dynamics and vibration suppression of space structures with control moment gyroscopes, Acta Astronautica 96 (1) (2014) 232–245. doi:10.6002/ect.2017.0308.
URL http://dx.doi.org/10.1016/j.actaastro.2013.11.032
[32] C. J. Damaren, G. M. T. D'Eleuterio, Optimal Control of Large Space Structures Using Distributed Gyricity, Journal of Guidance Control and Dynamics 12 (5) (1989) 723–731. doi:10.1108/13598540610652492.
[33] Y. Hu, Y. Geng, J. D. Biggs, Simultaneous Spacecraft Attitude Control and Vibration Suppression via Control Allocation, Journal of Guidance, Control, and Dynamics 44 (10) (2021) 1853–1861. doi:10.2514/1.g005834.

[34] M. Polites, J. Kalmanson, D. Mangus, Solar sail attitude control using small reaction wheels and magnetic torquers, Proceedings of the Institution of Mechanical engineers, Part G: Journal of Aerospace Engineering 222 (2007) 53–62. doi:10.1243/09544100JAERO250.
[35] M. Y. Ovchinnikov, D. S. Roldugin, A survey on active magnetic attitude control algorithms for small satellites, Progress in Aerospace Sciences 109 (August, 2019). doi:10.1016/j.paerosci.2019.05.006.
[36] M. Lovera, A. Astolfi, Spacecraft attitude control using magnetic actuators, Automatica 40 (8) (2004) 1405–1414. doi:10.1016/j.automatica.2004.02.022.
[37] Y. Yang, Controllability of spacecraft using only magnetic torques, IEEE Transactions on Aerospace and Electronic Systems 52 (2) (2016) 954–961. arXiv:1507.06963, doi:10.1109/TAES.2015.150520.
[38] A. Colagrossi, M. Lavagna, Fully magnetic attitude control subsystem for picosat platforms, Advances in Space Research 62 (12) (2018) 3383–3397. doi:10.1016/j.asr.2017.10.022.
[39] W. M. J. Robbins, The Feasibility of an Orbiting 1500-Meter Radiotelescope (NASA CR-792, 1967).
[40] O. Çelik, C. R. McInnes, An analytical model for solar energy reflected from space with selected applications, Advances in Space Research (2021). doi:10.1016/j.asr.2021.10.033.
URL https://doi.org/10.1016/j.asr.2021.10.033
[41] O. Çelik, A. Viale, T. Oderinwale, L. Sulbhewar, C. R. McInnes, Enhancing Terrestrial Solar Power Using Orbiting Solar Reflectors, 72nd International Astronautical Congress (IAC), Dubai, United Arab Emirates (2021). doi:10.1016/j.asr.2021.10.033.
[42] Y. Shirasawa, O. Mori, Y. Miyazaki, H. Sakamoto, M. Hasome, N. Okuizumi, H. Sawada, H. Furuya, S. Matsunaga, M. Natori, J. Kawaguchi, Analysis of membrane dynamics using multi-particle model for solar sail demonstrator "IKAROS", Collection of Technical Papers - AIAA/ASME/ASCE/AHS/ASC Structures, Structural Dynamics and Materials Conference (April) (2011) 3–4. doi:10.2514/6.2011-1890.
[43] T. L. Tien, in: Structural Engineering Handbook, CRC Press LLC, 1999, Ch. Space Frame Structures.
[44] K. Arun, T. Huang, S. Blostein, Least-Squares Fitting of Two 3-D Point Sets, IEEE Trans. Patt. Anal. Machine Intell., PAMI-9 (5) (1987) 698–699.
[45] L. Herbeck, C. Sickinger, M. Eiden, M. Leipold, Solar sail hardware developments, European Conference on Spacecraft Structures, Materials and Mechanical Testing (2002) 1–10.
[46] Magnetorquer rod datasheet, newspace systems (Online Datasheet, Retrieved 2 October 2019).
URL http://www.newspacesystems.com/wp-content/uploads/2018/10/NewSpace-Magnetorquer-Rod_7b.pdf
[47] T. W. Murphey, Symbolic equations for the stiffness and strength of straight longeron trusses, Collection of Technical Papers - AIAA/ASME/ASCE/AHS/ASC Structures, Structural Dynamics and Materials Conference 9 (0704) (2006) 6298–6311. doi:10.2514/6.2006-2123.
[48] J. J. Kim, B. N. Agrawal, Experiments on jerk-limited slew maneuvers of a flexible spacecraft, Collection of Technical Papers - AIAA Guidance, Navigation, and Control Conference 2006 2 (August) (2006) 1030–1049. doi:10.2514/6.2006-6187.
[49] G. Fracchia, J. D. Biggs, M. Ceriotti, Analytical low-jerk reorientation maneuvers for multi-body spacecraft structures, Acta Astronautica 178 (April 2020) (2021) 1–14. doi:10.1016/j.actaastro.2020.08.020.
URL https://doi.org/10.1016/j.actaastro.2020.08.020
[50] J. C. Urschel, On the characterization and uniqueness of centroidal voronoi tessellations, SIAM Journal on Numerical Analysis 55 (3) (2017) 1525 – 1547. doi:10.1137/15m1049166.
[51] J. Burns, Centroidal voronoi tesseletions (Online, Retrieved 10 October 2019).
URL https://www.whitman.edu/Documents/Academics/Mathematics/burns.pdf
[52] S. P. Lloyd, Least squares quantization in pcm, IEEE Transactions on Information Theory 28 (2) (1982) 129–137. doi:10.1109/TIT.1982.1056489.
[53] Q. Du, V. Faber, M. Gunzburger, Centroidal voronoi tessellations: Applications and algorithms, SIAM Review 41 (4) (2005) 637–676. doi:10.1137/s0036144599352836.
[54] M. J. Sidi, Spacecraft Dynamics and Control: A Practical Engineering Approach, Cambridge University Press, Cambridge, 1997, pp. 88–111. doi:10.1017/CBO9780511815652.
[55] NASA, State of the Art of Small Spacecraft Technology, Tech. Rep. December (2018).
URL https://sst-soa.arc.nasa.gov/04-propulsion
[56] A. S. Stickler, A magnetic control system for attitude acquisition (NASA CR-130145, January 1972).
[57] B. M. Chulliat, A., W. Brown, P. Alken, C. Beggan, M. Nair, G. Cox, A. Woods, S. Macmillan, M. Paniccia, The US / UK World Magnetic Model for 2020-2025, Tech. rep. (2020). doi:10.25923/ytk1-yx35.